

From Physics Constraints to Trustworthy Bayesian Reasoning: Synergies of PINN, iPINN, and iBPINN in Prestack AVO Inversion

Zhen Liu^{ID}, Junhua Zhang^{ID}, Yongrui Chen, Deyong Feng, and Liang Qi

Abstract—Physics-informed neural networks (PINNs) enable unsupervised inversion by integrating seismic forward modeling equations directly into neural network loss functions, operating on angle-domain seismic data. The inverse PINN (iPINN) extends this framework by treating the central frequency of the Ricker wavelet as a trainable parameter, thereby enhancing the adaptability to spectral mismatch and improving lateral continuity in inversion results. However, iPINN do not provide uncertainty quantification for their predictions. To address this limitation, an inverse Bayesian PINN (iBPINN) is proposed, incorporating Flipout-based Bayesian convolutional and fully connected layers into the iPINN architecture. Through the variational inference, iBPINN enables the probabilistic modeling of both network weights and wavelet frequency, yielding not only predicted physical parameters but also posterior standard deviation (std) maps for direct visualization and quantitative assessment of predictive uncertainty. Numerical experiments on the Marmousi synthetic model show that PINN achieves rapid convergence for large-scale stratigraphic structures, while iPINN provides more consistent inversion results for deeper layers and weakly sensitive parameters via dynamic frequency correction. iBPINN maintains comparable inversion consistency and, crucially, enables intuitive mapping of predictive uncertainty through std analysis, particularly in fault zones, high-impedance contrasts, and low-signal-to-noise ratios (SNR) regions. Field application to seismic data from a CO₂ injection site further demonstrates that the uncertainty maps provided by iBPINN offer additional insights into fluid substitution and reservoir connectivity. This methodological progression—from PINN (“statistics + logic”) to iPINN (“logic + adaptability”), and ultimately to iBPINN (“logic + reasoning”)—mirrors the broader evolution of artificial intelligence (AI) in geophysical inversion: from statistical models to logic-embedded frameworks, and finally to reasoning-enhanced architectures. The proposed iBPINN framework, thus, offers a unified, interpretable, and trustworthy approach for next-generation seismic inversion in complex geological environments.

Index Terms—Bayesian layer, inverse Bayesian PINN (iBPINN), inverse PINN (iPINN), physics-informed neural

Received 13 January 2025; revised 11 June 2025, 17 September 2025, and 26 October 2025; accepted 20 November 2025. Date of publication 24 November 2025; date of current version 16 December 2025. This work was supported by the Geophysical Research Institute, Sinopec Shengli Oilfield Company, through the Project “Research on CO₂ Flooding Non-Uniformity Time-Lapse Seismic Monitoring Technology” under Grant 30200020-23-ZC0613-0023. (*Corresponding author:* Junhua Zhang.)

Zhen Liu, Junhua Zhang, and Yongrui Chen are with the National Key Laboratory of Deep Oil and Gas and the School of Geosciences, China University of Petroleum (East China), Qingdao, Shandong 266580, China (e-mail: lincoln110@foxmail.com; zjh@upc.edu.cn; 348308670@qq.com).

Deyong Feng and Liang Qi are with the Geophysical Research Institute, Sinopec Shengli Oilfield Company, Dongying, Shandong 257022, China (e-mail: martineredingerjuv74@gmail.com; vegac3120@gmail.com).

Digital Object Identifier 10.1109/TGRS.2025.3636416

network (PINN), prestack amplitude variations with offset (AVO) inversion, uncertainty quantification.

I. INTRODUCTION

THE seismic inversion can be classified into poststack and prestack inversion. Poststack data, processed using stacking techniques, lose critical information about amplitude variations with offset (AVO) or amplitude variations with angle (AVA). In contrast, the prestack data retain more of the original seismic information, making them uniquely advantageous for inverting P-wave velocity, S-wave velocity, density, and elastic parameters such as Poisson’s ratio and Lamé coefficients [1].

In recent years, the prestack AVO inversion has emerged as a core technology for reservoir characterization. Grana et al. [2] noted that due to the limited frequency bandwidth of seismic data, as well as noise interference and variations in processing techniques, seismic inversion is typically an overdetermined problem. It is characterized by nonuniqueness and instability, rendering direct solutions infeasible. Koefoed [3] investigated the impact of lithological parameters, especially Poisson’s ratio, on the plane wave reflection coefficient. This study overcame the assumption made by Muskat and Meres [4], which considered Poisson’s ratio a constant, and was the first to identify Poisson’s ratio as a key factor influencing AVA, highlighting its potential as a lithology indicator. The approximate formula of the Zoeppritz equations derived by Aki and Richards [5] significantly advanced the development of inversion techniques by providing an analytically tractable expression for angle-dependent P–P reflection coefficients. Its linearized form enabled gradient-based inversion and became a foundation for modern AVO analysis. However, the approximation assumes small incidence angles and weak elastic contrasts, which limits its accuracy in high-contrast or wide-angle scenarios. Buland et al. [6] introduced a Bayesian linear prestack AVO inversion method, improving the inversion accuracy.

Traditional prestack inversion methods often begin with constructing an initial model and then solving the seismic inverse problem using optimization algorithms. Early AVO inversion approaches primarily relied on linearized methods [7], followed by the development of various nonlinear techniques [8], [9]. Gradient-based local optimization algorithms (e.g., Gauss–Newton and conjugate gradient) are widely used but are known to be highly sensitive to the quality of the initial

model and often require significant computational resources due to repeated forward simulations.

To mitigate these shortcomings, global optimization methods—such as genetic algorithms, simulated annealing, and particle swarm optimization—have been applied successfully in geophysical inversion to reduce dependence on initial models and better handle complex, multimodal search spaces. For instance, the study by Kant et al. [10] demonstrated particle swarm optimization (PSO) and genetic algorithm (GA) yielding accurate reservoir impedance and porosity predictions on real Blackfoot field data. Another recent work by Yuan et al. [11] improved wavelet estimation and inversion stability using PSO in a multiwell synchronized framework. However, these global methods remain computationally demanding, especially for high-dimensional prestack seismic inversion with limited frequency content.

The rapid advancements in computer hardware, particularly in processor speed, parallel computing capabilities, and storage capacity, have led to the resurgence of neural network algorithms, which are now widely applied across multiple domains. These technological advances have enabled deep learning models, previously considered computationally expensive, to run efficiently and effectively. Deep learning techniques have become a cornerstone of modern artificial intelligence (AI), finding broad applications in image recognition, natural language processing, and autonomous driving, among other fields, driving innovation and transformation in numerous industries. Given their exceptional learning capabilities, deep learning algorithms have increasingly been adopted by geophysicists to address challenges in seismic inversion. Alfarraj and AlRegib [12] proposed a semi-supervised modeling framework based on recurrent neural networks to predict elastic impedance from prestack angle data. Das et al. [13] utilized convolutional neural networks to extract seismic impedance parameters. However, a limitation of data-driven algorithms is their dependency on large training datasets, meaning the success of neural network applications hinges significantly on the availability of abundant training data [14], [15], [16].

Over time, empirical, theoretical, and computational paradigms have accumulated extensive knowledge, including physical laws, mechanism analysis, and expert experience. In deep learning, these are collectively referred to as physical knowledge or physical information. Combining physical information with deep learning has given rise to emerging research directions such as physics-guided deep learning (PGDL) and theory-guided deep learning (TGDL). These approaches embed domain-specific physical principles into models, enhancing their interpretability and physical consistency while reducing reliance on large-scale observational data [17]. Although attempts to incorporate the prior knowledge into neural networks date back to the 1990s [18], the development of physics-informed neural networks (PINNs) began in 2017 with Raissi et al. [19], [20], who constrained deep learning algorithms with physical equations to solve partial differential equations. These studies have not only explored the potential of PGDL but also provided theoretical and practical foundations for its application across disciplines. In recent years, numerous researchers have further refined

PGDL methods, achieving significant breakthroughs in various fields [21], [22], [23], [24], validating its potential to enhance the model accuracy, generalization, physical consistency, and robustness.

In recent years, the significant progress has been made in applying PINNs to the forward and inverse modeling of geophysical wave equations. Rasht-Behesht et al. [25] were among the first to implement PINNs for solving the 2-D acoustic wave equation and full-waveform inversion (FWI). By leveraging the automatic differentiation, they precisely enforced absorbing boundary conditions and utilized the grid-independence and compact coding of PINNs to enhance the simulation flexibility and computational efficiency in complex geological structures. Song et al. [26] proposed a PINN-based solution for the acoustic wave equation in vertical transverse isotropy (VTI) media. Their method bypassed the bottleneck of impedance matrix inversion through automatic differentiation and demonstrated feasibility and efficiency for anisotropic media within 3-D irregular topography models. Wu et al. [27] introduced the second-order derivatives and smoothed perfectly matched layer (PML) conditions into PINNs for Helmholtz equations in nonsmooth media. By enforcing absorbing layer losses and employing quadratic activation functions, they significantly improved the simulation accuracy in complex terrain settings. The latest development, multiscale Fourier feature PINN (MFF-PINN), was proposed by Chai et al. [28]. This method jointly encodes spatial coordinates, source positions, and frequencies using adaptive activation functions, effectively mitigating the spectral bias in high-frequency scenarios and achieving high-precision predictions of multisource and multifrequency wavefields.

PINNs have also demonstrated strong potential in traveltime modeling and tomography. Waheed et al. [29] developed the PINNeik algorithm, which directly trains networks to output first-arrival traveltimes by enforcing the Eikonal residual as a hard constraint. This approach was successfully applied to the phase velocity tomography of Rayleigh and Love waves, yielding high-resolution velocity models. Chen et al. [30] proposed a PINN-based traveltime tomography method for Rayleigh waves, where physical constraints guided parameter optimization, effectively reducing the influence of noise and enhancing imaging accuracy. Grubas et al. [31] introduced the neural Eikonal solver (NES), which incorporates an improved factorization strategy, Gaussian activation functions, and asymmetric loss functions. NES efficiently addressed caustic-related challenges in velocity models, reducing traveltime errors by a factor of 1–60 compared with traditional fast marching methods. In terms of uncertainty quantification, promising advances have also been reported. Yang et al. [32] introduced Bayesian reasoning into the PINN framework by proposing Bayesian PINNs (B-PINNs), which probabilistically modeled network weights using variational inference. This enabled quantification of solution uncertainty in both forward and inverse problems, showing strong robustness under noisy data and uncertain prior conditions. Building on this, Gou et al. [33] proposed B-PINNs for Eikonal-based inversion, integrating Gaussian variational inference and Stein variational gradient descent (SVGD). Their approach enabled joint inversion of

traveltimes and velocity fields with uncertainty estimation, providing reliable confidence intervals without requiring an initial model. Biswas et al. [34] introduced PINN to geophysical inversion by successfully implementing both prestack and poststack inversion. Song and Alkhalifah [35] applied PINN for wavefield reconstruction inversion (WRI), demonstrating that PINN-based WRI can produce reasonable velocity models with limited iterations and frequency inputs, making it suitable for subsequent FWI applications.

AI is undergoing a methodological evolution from “statistics-driven” to “logic-driven,” and further toward a hybrid paradigm of “logic combined with reasoning.” In the context of seismic inversion, particularly AVO inversion, a similar trajectory can be observed: traditional data-fitting algorithms are gradually being replaced by models incorporating physical constraints, ultimately advancing toward intelligent inversion systems capable of reasoning and uncertainty quantification.

The PINN, inverse PINN (iPINN), and inverse Bayesian PINN (iBPINN) methods proposed in this study exemplify three typical stages along this evolutionary path. The conventional neural network inversion methods rely on supervised learning using data-label pairs, allowing the model to capture numerical correlations but not the underlying physical or logical relationships. This stage is, therefore, referred to as the “statistics-fitting phase.” In contrast, the PINN couples the Zoeppritz equations into the loss function, enforcing physical laws during the training process. This transforms the model from a purely statistical learner into a “logic-driven” system that ensures the physical consistency while fitting the observed data. However, PINNs still yield deterministic point estimates based on fixed network weights.

Building upon this framework, iPINN introduces the wavelet’s central frequency as a trainable parameter, enabling dynamic optimization of the forward modeling frequency. This enhancement reduces reliance on manually tuned priors and improves robustness against observation and modeling errors. While iPINN retains physical constraints and introduces a degree of adaptiveness, its reasoning capability remains limited. Specifically, iPINN can self-adjust wavelet frequency and enforce physically meaningful outputs, but it cannot characterize the distributional uncertainty of its predictions. As such, it represents a transitional form between “logic-driven” and “logic + reasoning” paradigms, falling short of full-Bayesian posterior inference.

To overcome this limitation, iBPINN integrates a Bayesian reasoning framework into the PINN architecture by treating both the elastic parameters and wavelet frequency as probabilistic variables. Through the variational inference, the model learns posterior distributions conditioned on prior beliefs and observed data. This not only provides mean predictions but also quantifies predictive uncertainty via posterior variance or credible intervals. Such a Bayesian update mechanism equips the model with the ability to dynamically revise its internal belief states, effectively realizing the “logic + reasoning” stage. This substantially enhances the reliability and interpretability of inversion results.

In summary, the methodological progression from PINN to iPINN to iBPINN mirrors the broader AI evolution from deterministic logic to logic fused with reasoning. This trajectory enhances consistency and robustness of AVO inversion and offers a viable paradigm for developing geophysical intelligent inversion systems that integrate knowledge representation, uncertainty quantification, and logical inference—offering both theoretical insights and practical applications.

II. METHODS

A. PINN/iPINN Network Architecture

As illustrated in Fig. 1(a), the PINN takes prestack angle gathers at near-, mid-, and far-incidence angles as input. It first employs three sets of convolutional kernels (Kernel1–Kernel3) to extract local semantic features from each angle gather. Each convolutional stream consists of a convolutional layer followed by batch normalization, rectified linear unit (ReLU) activation, and dropout, ensuring the stable feature extraction and mitigating overfitting. The outputs of the convolutional layers are passed through several fully connected layers to estimate the spatial distributions of subsurface physical parameters: P-wave velocity (V_P), S-wave velocity (V_S), and density (ρ).

The predicted V_P , V_S , and ρ are fed into a forward modeling module based on the Zoeppritz equations to compute the P–P reflection coefficients at corresponding incident angles. This module establishes a differentiable mapping from elastic parameters to angle-domain seismic responses. Subsequently, these reflection coefficients are convolved in the time domain with a Ricker wavelet to generate synthetic angle gathers. The mean squared error (mse) between the synthetic and observed angle gathers serves as the data-fitting term in the loss function. Combined with a physics-consistency term derived from the Zoeppritz equations, this enables unsupervised inversion of the elastic parameters.

Building upon the PINN framework, the iPINN enhances adaptability by treating the central frequency f_0 of the Ricker wavelet as a trainable parameter and introducing a frequency regularization term into the loss function. The overall network architecture remains similar: multiangle gathers are processed through convolution–BatchNorm–ReLU–dropout layers to extract local features, followed by fully connected layers that output V_P , V_S , and ρ . These predictions are then used to compute reflection coefficients, which are convolved with a dynamically optimized Ricker wavelet to produce the synthetic seismic data.

The key distinction is that iPINN models f_0 as a trainable variable rather than a fixed prior, thereby avoiding the spectral mismatch caused by manually preset wavelets. During training, both the elastic parameters and the central frequency f_0 are simultaneously updated through backpropagation.

B. IBPINN for Trustworthy Seismic Inversion

To further enhance the robustness, credibility, and representational capacity of PINNs in seismic inversion tasks, this study proposes an improved model—iBPINN—which integrates the Bayesian uncertainty modeling into the iPINN

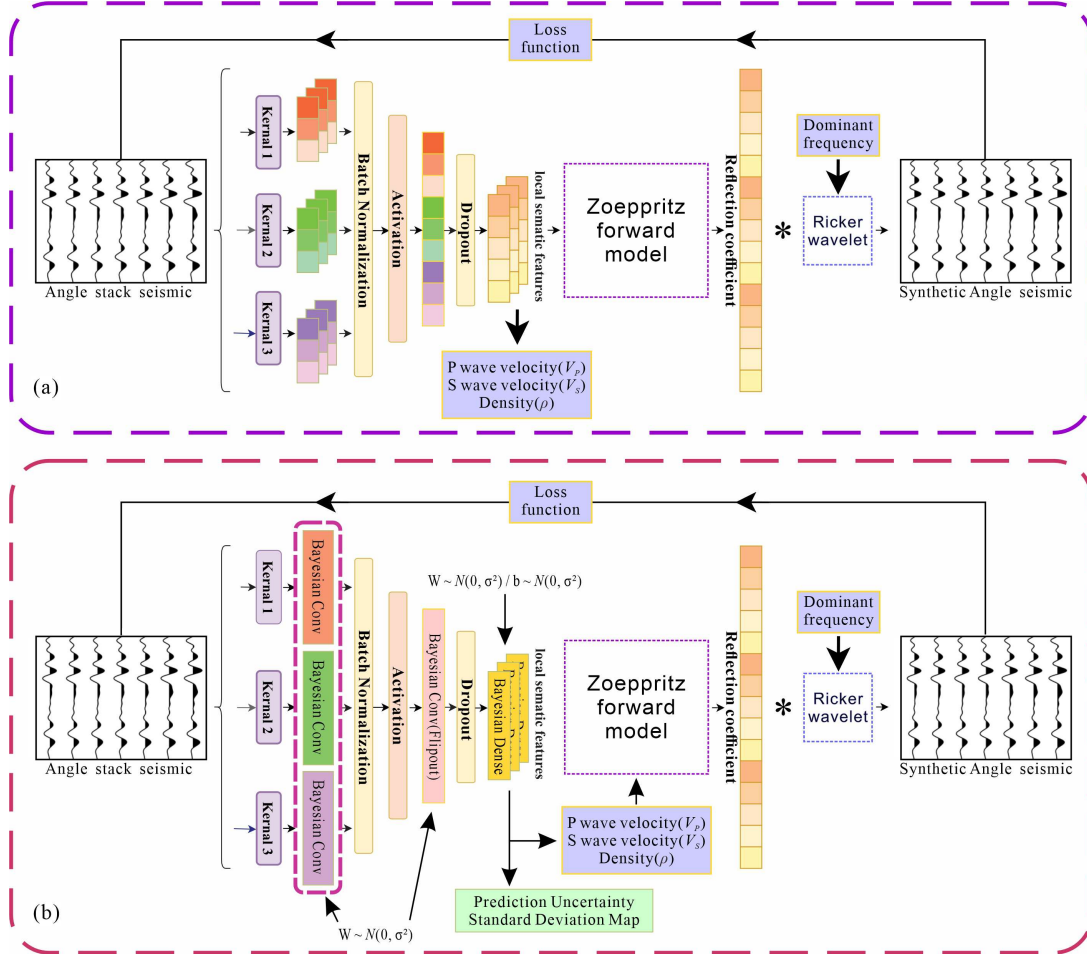


Fig. 1. (a) PINN/iPINN and (b) iBPINN network architecture.

framework. While retaining the adaptive wavelet frequency optimization capability of iPINN, iBPINN introduces a Bayesian neural network architecture to perform the probabilistic modeling of the network parameters. This allows explicit estimation of inversion uncertainty and incorporates Kullback–Leibler (KL) divergence regularization to control model complexity, thereby improving the prediction stability and reliability under complex geological conditions and noisy data scenarios.

Specifically, iBPINN replaces the deterministic convolutional and fully connected layers in iPINN with Bayesian layers. Unlike conventional neural networks, in which weights and biases are fixed scalars, Bayesian networks treat each parameter as a probability distribution (typically Gaussian), and training is conducted by maximizing the evidence lower bound (ELBO) via variational inference. The prior distribution of the weights is usually set as a zero-mean Gaussian with a standard deviation (std) of $\sigma = 0.1$, while the posterior distribution is learned through optimization during training.

Flipout, an efficient Bayesian sampling technique, is employed to decorrelate weight samples during forward passes. By perturbing parameters using Rademacher vectors, Flipout enables posterior sampling without explicitly instantiating multiple sample paths, significantly reducing gradient

variance and improving the computational efficiency. As a result, each forward pass in iBPINN involves a different set of sampled network parameters, allowing the model to generate both the mean prediction (denoted by mean) and std estimate (denoted by std) for each physical parameter. The former represents the most probable inversion result, while the latter quantifies predictive uncertainty.

The network input consists of seismic angle gathers with shape $(3, T, 1)$, corresponding to near, mid, and far offsets. Local seismic features are first extracted using a Bayesian convolutional layer with 16 kernels of size 1×60 and a stride of 1×2 , operating along the time axis to capture waveform details. The convolutional output is batch-normalized to enhance the training stability, activated via ReLU to introduce nonlinearity, and regularized using a dropout rate of 0.3 to mitigate overfitting.

Next, the extracted features are flattened and passed through a Bayesian fully connected layer that outputs a $(3 \times T)$ vector representing the spatial distributions of the three target geophysical parameters: P-wave velocity (V_p), S-wave velocity (V_s), and Density (ρ). The outputs are scaled to the $[1]$ range using a sigmoid activation function and reshaped back to a $(3, T)$ format corresponding to the physical model structure.

Training is performed using TensorFlow's automatic differentiation mechanism, enabling joint optimization of network parameters and wavelet frequency. A dynamic learning rate scheduler is used to accelerate convergence. Because the network outputs not only the mean predictions but also pointwise std estimates, credible interval maps (mean \pm std) can be generated, providing valuable uncertainty quantification for applications such as reservoir characterization and CO₂ sequestration monitoring.

In summary, iBPINN extends the iPINN framework by incorporating Bayesian modeling, enabling simultaneous optimization of wavelet frequency, seismic parameter prediction, and uncertainty estimation. Compared with conventional PINN and iPINN approaches, iBPINN is better suited for inversion tasks under high-noise conditions, unknown frequency content or scenarios requiring trustworthy decision support. It represents a high-robustness, high-reliability reasoning-oriented neural network architecture aligned with the demands of next-generation seismic inversion.

C. Physical Constraints

In PINN and its extended models, the incorporation of a forward physical modeling module is a critical component for enabling unsupervised inversion. To ensure that the network outputs carry clear physical meaning and can be used to generate seismic records through inversion, this study employs a P-P reflection coefficient model based on the Zoeppritz equation, combined with a frequency-differentiable Ricker wavelet construction function. This design enables an end-to-end forward modeling process from elastic parameters to angle-domain synthetic seismic records.

At the interface between two adjacent layers, let the P-wave velocity, S-wave velocity, and density be denoted as (V_{P1} , V_{S1} , and ρ_1) and (V_{P2} , V_{S2} , and ρ_2) for the upper and lower media, respectively, with an incident angle of θ_1 . According to the approximate form of the Zoeppritz equation, the P-P reflection coefficient R_{PP} can be expressed as follows:

$$R_{PP} = \frac{Z_2 \cos \theta_2 - Z_1 \cos \theta_1}{Z_2 \cos \theta_2 + Z_1 \cos \theta_1} \quad (1)$$

where $Z_1 = \rho_1 V_{P1}$ and $Z_2 = \rho_2 V_{P2}$ are the acoustic impedances of the upper and lower layers, respectively. θ_2 is the transmitted angle, which can be determined according to Snell's law

$$\sin \theta_2 = \frac{V_{P2}}{V_{P1}} \sin \theta_1. \quad (2)$$

This computation is implemented in a tensorized form in this study, enabling parallel calculation of reflection coefficients across multiple samples and incident angles.

To incorporate the wavelet generation process into network training and enable end-to-end frequency optimization, the dominant frequency f_0 of the Ricker wavelet is defined as a trainable variable. Its time-domain expression is

$$w(t; f_0) = (1 - 2\pi^2 f_0^2 t^2) \cdot \exp(-\pi^2 f_0^2 t^2) \quad (3)$$

where t denotes the time axis and f_0 is automatically optimized by the network. This function is implemented in a fully

tensorized structure to ensure the frequency gradient remains differentiable and can be propagated during training.

Finally, the model generates synthetic seismic records by performing a 1-D convolution between the reflection coefficient series and the wavelet

$$S_{\text{syn}}(\theta, t) = R_{PP}(\theta) * w(t; f_0) \quad (4)$$

where S_{syn} represents the synthetic seismic record, $*$ denotes the 1-D convolution operation, and θ is the incident angle. To match the observed records, the length of the synthetic data is truncated according to the target number of time steps T , and a normalization is applied using fixed minimum and maximum values

$$\hat{S}_{\text{syn}} = \frac{S_{\text{syn}} - S_{\min}}{S_{\max} - S_{\min}}. \quad (5)$$

Here, \hat{S}_{syn} denotes the normalized synthetic seismic trace, and S_{\max} and S_{\min} are normalization constants determined via global scanning prior to training.

In summary, iBPINN incorporates a physically consistent modeling path by embedding the Zoeppritz equation-based constraints and a differentiable Ricker wavelet generator into the network architecture. This enables the neural network to simulate the physical process of seismic wave propagation and reflection. The entire physical modeling pathway remains differentiable during forward propagation, thereby providing a physics-consistent loss signal for unsupervised inversion. This design forms a solid foundation for the seamless integration of data-driven learning and theory-driven modeling.

D. PINN/iPINN Loss Function

The loss function design of PINN is based on two aspects: physical constraints and data consistency. For seismic inversion problems, the goal of PINN is to predict subsurface physical parameters, such as P-wave velocity (V_P), S-wave velocity (V_S), and density (ρ), through a neural network, and compare these parameters with the seismic data's reflection characteristics to achieve high-precision parameter inversion. The PINN loss function comprises the following two components.

Data-Fitting Loss: This component evaluates the model's predictive capability by comparing the synthetic seismic data generated by the network with the actual input seismic data. Using the Zoeppritz equation and input angle gather seismic data, reflection coefficients are calculated to generate synthetic seismic records. The mse between the actual seismic data and the generated synthetic data is then computed

$$L_{\text{data}} = \frac{1}{N} \sum_{i=1}^N \left(S_{\text{pred}}^{(i)} - S_{\text{true}}^{(i)} \right)^2 \quad (6)$$

where S_{pred} represents the synthetic seismic data generated by the model, S_{true} is the actual seismic data, and N is the number of samples.

In seismic data inversion, the lateral continuity of subsurface properties is an important physical characteristic. Therefore,

PINN incorporates first-order and second-order derivative regularization terms to constrain the lateral continuity of the model's predicted results

$$L_{\text{grad}} = \lambda_1 \cdot \frac{1}{N} \sum_{i=1}^N \left(P_{j+1}^{(i)} - P_j^{(i)} \right)^2 \quad (7)$$

$$L_{\text{second-grad}} = \lambda_2 \cdot \frac{1}{N} \sum_{i=1}^N \left(P_{j+2}^{(i)} - 2P_{j+1}^{(i)} + P_{j+1}^{(i)} \right)^2 \quad (8)$$

where $P_j^{(i)}$ represents the model's predicted value at lateral position j and λ_1 and λ_2 are the regularization weights. Note that this second-order term is not related to Hessian-based optimization, but is introduced purely as a smoothness regularization constraint.

To further stabilize the inversion and introduce prior geological information, a model constraint term is added to penalize large deviations from a smoothed initial model. This term is defined as follows:

$$L_{\text{prior}} = \lambda_3 \cdot \frac{1}{N} \sum_{i=1}^N \left(P^{(i)} - P_{\text{init}}^{(i)} \right)^2 \quad (9)$$

where $P_{\text{init}}^{(i)}$ denotes the value from the smoothed initial model and λ_3 controls the strength of this constraint.

The final total loss function of PINN is

$$L_{\text{PINN}} = L_{\text{data}} + L_{\text{grad}} + L_{\text{second-grad}} + L_{\text{prior}}. \quad (10)$$

iPINN extends the loss function design of PINN by introducing a dynamic frequency optimization mechanism, enhancing the model's adaptability under conditions of wavelet dominant frequency uncertainty. The iPINN loss function adds a frequency optimization constraint term to the PINN framework.

In iPINN, the wavelet dominant frequency is defined as a learnable parameter that is automatically optimized during model training to approximate the target frequency. The corresponding regularization term is defined as follows:

$$L_{\text{freq}} = \lambda_4 \cdot (f_{\text{preq}} - f_{\text{target}})^2 \quad (11)$$

where f_{preq} is the dominant frequency optimized during training, f_{target} is the target frequency, and λ_4 is the frequency regularization weight.

The total loss function of iPINN includes the data-fitting loss, lateral continuity constraints, and the frequency optimization term

$$L_{\text{PINN}} = L_{\text{data}} + L_{\text{grad}} + L_{\text{second-grad}} + L_{\text{prior}} + L_{\text{freq}}. \quad (12)$$

Through this design, iPINN not only retains the physical constraint characteristics of PINN but also enhances the model's flexibility and robustness by dynamically adjusting the wavelet dominant frequency. This approach improves the inversion consistency and stability, particularly under conditions of frequency uncertainty or complex geological scenarios.

E. iBPINN Loss Function

The total loss function of iBPINN consists of five components: data-fitting loss, model prior loss, spatial smoothness regularization, frequency matching term, and the Bayesian regularization term (KL divergence). The complete formulation is expressed as follows:

$$L_{\text{iBPINN}} = L_{\text{data}} + L_{\text{grad}} + L_{\text{second-grad}} + L_{\text{freq}} + \beta_t \cdot L_{\text{KL}}. \quad (13)$$

The first four components are identical to those used in iPINN. Specifically, they ensure accurate data-to-synthetic matching, consistency between predicted results and the geological prior model, lateral continuity of inverted parameters, and dynamic adjustment of the wavelet's central frequency. The final component—the KL divergence term—is unique to iBPINN and is introduced to constrain the posterior distributions of Bayesian network parameters from deviating excessively from their predefined priors.

Notably, iBPINN adopts a KL divergence annealing strategy during training. Since the KL term may impose overly strong regularization in the early training stages—potentially hindering the network's capacity to explore optimal solutions—this study employs a temporal annealing scheme to gradually increase the KL weight. Initially, a small KL coefficient is used, which is then progressively ramped up to its target value. The annealing coefficient β_t is defined as follows:

$$\beta_t = \min \left(1, \frac{t}{T_{\text{anneal}}} \right). \quad (14)$$

Here, t denotes the current training epoch, and T_{anneal} represents the total number of epochs over which the KL weight is gradually increased. This annealing mechanism enables a dynamic balance among the physics-based term, data fidelity term, and Bayesian regularization term within the loss function, thereby enhancing the network's stability and representational capacity.

Upon completion of training, iBPINN further supports explicit quantification of inversion uncertainty, a capability made possible by the parameter sampling mechanism provided by the Flipout structure in the Bayesian network. During inference, multiple forward passes are performed for the same input x_i by sampling weight parameters $w^{(s)} \sim q(w)$ from the learned posterior distribution

$$\hat{y}_i^{(s)} = f(x_i; w^{(s)}), \quad s = 1, 2, \dots, S. \quad (15)$$

The final prediction is obtained by computing statistical moments over all sampled outputs, specifically the predictive mean and std, as follows:

$$\mu_i = \frac{1}{S} \sum_{s=1}^S \hat{y}_i^{(s)}, \quad \sigma_i = \sqrt{\frac{1}{S-1} \sum_{s=1}^S \left(\hat{y}_i^{(s)} - \mu_i \right)^2}. \quad (16)$$

Here, μ_i represents the expected value (mean) of the inversion result at location i , while σ_i quantifies the predictive uncertainty at that point. The term $\hat{y}_i^{(s)}$ denotes the network's prediction for input x_i under the s th sampled set of weights. A smaller std indicates higher prediction stability and reliability, whereas a larger std may reflect data sparsity or complex geological features in the corresponding region.

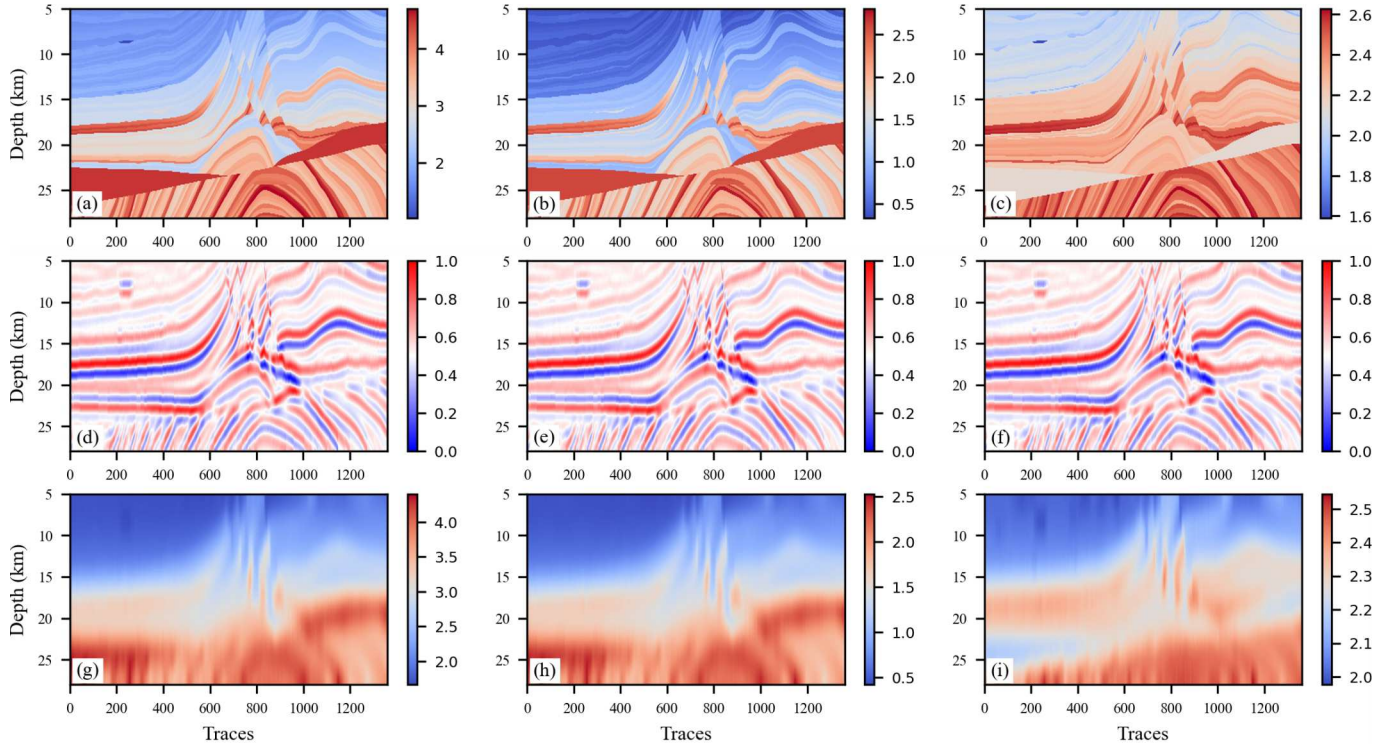


Fig. 2. Marmousi2 model, corresponding synthetic seismic angle gathers, and low-frequency initial models. (a) P-wave velocity. (b) S-wave velocity. (c) Density model. (d) Near-angle synthetic seismic data. (e) Mid angle. (f) Far angle. (g) Low-frequency initial model of P-wave velocity. (h) Low-frequency initial model of S-wave velocity. (i) Low-frequency initial model of density.

This procedure is essentially a Monte Carlo approximation to Bayesian inference, enabling the construction of credible interval maps ($\text{mean} \pm \text{std}$) for seismic parameters. Such uncertainty visualization assists geoscientists in identifying potentially anomalous regions, providing reliable decision support for tasks such as hydrocarbon exploration, carbon sequestration, and reservoir modeling.

In conclusion, iBPINN extends the learnable frequency framework of iPNN by incorporating KL regularization and uncertainty quantification. This not only enhances the model's robustness and adaptability under complex subsurface conditions but also provides a quantitative measure of confidence for the inversion results. It marks a significant step forward from purely physics-driven deep learning to a “logic + reasoning” paradigm, laying the groundwork for trustworthy AI-based seismic inversion guided by physical priors.

III. NUMERICAL EXAMPLES

A. Generating Training Data

In this study, the training dataset was constructed using the Marmousi2 model, a benchmark in seismic research known for its high-resolution subsurface parameter distributions, including V_p , V_s , and ρ [see Fig. 2(a)–(c)]. To accelerate computation and more clearly demonstrate the advantages of the proposed PINN-based AVO inversion framework, both the lateral and vertical sampling of the Marmousi2 model were reduced to one-tenth of the original resolution. Although the Marmousi2 model is provided in the depth domain, in this work, it is approximately treated as a time-equivalent model,

allowing for direct convolution with the Ricker wavelet to generate synthetic seismic records. This simplification does not affect the validity or effectiveness of the proposed method.

Synthetic seismic data were generated in the angle domain using the Zoeppritz equation, which facilitates the modeling of angular reflectivity. Three representative incident angles— 10° , 20° , and 30° —were selected to emulate seismic responses across a practical range of reflection scenarios commonly encountered in field surveys. A Ricker wavelet with a central frequency of 15 Hz and a total length of 64 points was employed to replicate the source signature. Convolution of this wavelet with the subsurface elastic property contrasts produced synthetic gathers corresponding to near, mid, and far angles [see Fig. 2(d)–(f)]. These simulated seismic records served as input for training both PINN and iPINN. By integrating the physically grounded Marmousi2 model and the Zoeppritz-based forward modeling framework, the resulting training data preserved physical consistency and offered high-fidelity samples for subsequent inversion tasks.

To provide a baseline for inversion and highlight the performance of different methods, low-frequency initial models of P-wave velocity, S-wave velocity, and density were also generated via appropriate smoothing operations [see Fig. 2(g)–(i)]. These initial models are used both as a prior in the inversion process and as a reference for comparison in subsequent analysis.

Fig. 3 presents the frequency spectrum analysis of the Marmousi2 synthetic seismic data at three representative incident angles (10° , 20° , and 30°). The dominant frequencies of all three gathers are observed to be centered around 15 Hz,

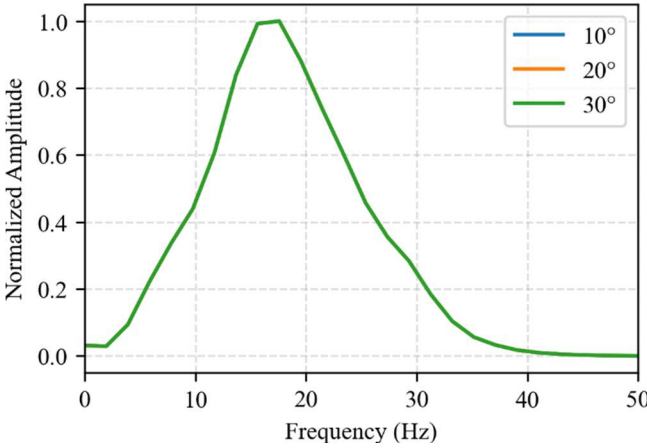


Fig. 3. Frequency spectrum analysis of Marmousi2 synthetic seismic data.

which is consistent with the Ricker wavelet frequency used in forward modeling. This validates the choice of 15 Hz as the target frequency for subsequent inversion procedures, and this value is adopted as the initial reference for frequency optimization in iPINN and iBPINN.

It should be noted that while the synthetic seismic data were generated using a fixed 15-Hz Ricker wavelet, this frequency serves only as a prior reference in the inversion stage. In the iPINN and iBPINN frameworks, the wavelet's dominant frequency is treated as a trainable parameter and is dynamically optimized during training to minimize the total loss. In addition, the above simplifications—including depth-to-time equivalence and decimation—are widely adopted for benchmarking neural network inversion frameworks. The primary aim of this study is to highlight the adaptability and uncertainty quantification capabilities of the proposed PINN-based methods, rather than to replicate precise field-scale seismic workflows. The initial models are constructed by low-pass filtering to preserve only the large-scale structural trends, providing a realistic and challenging baseline for inversion. While the dominant frequency in the synthetic data matches the wavelet frequency by design, this serves as a controlled validation scenario for the network's frequency adaptation mechanism. Future studies will consider more complex settings, including variable wavelets and explicit depth-to-time mapping, to further evaluate the robustness of the method.

B. Inversion Performance

Fig. 4 shows the training loss curves of the three methods—PINN, iPINN, and iBPINN—during the inversion of Marmousi2 synthetic seismic data as a function of training epochs. As observed, PINN [see Fig. 4(a)] exhibits a rapid decrease in loss at the early stage of training, achieving convergence within approximately 20 iterations, with the final loss remaining stable at a low level (below 0.005). This demonstrates the efficient convergence of the conventional PINN when the wavelet frequency is fixed and known.

In contrast, the loss reduction process for iPINN [see Fig. 4(b)] is relatively more gradual, and the overall convergence rate is slower than that of PINN, with the loss

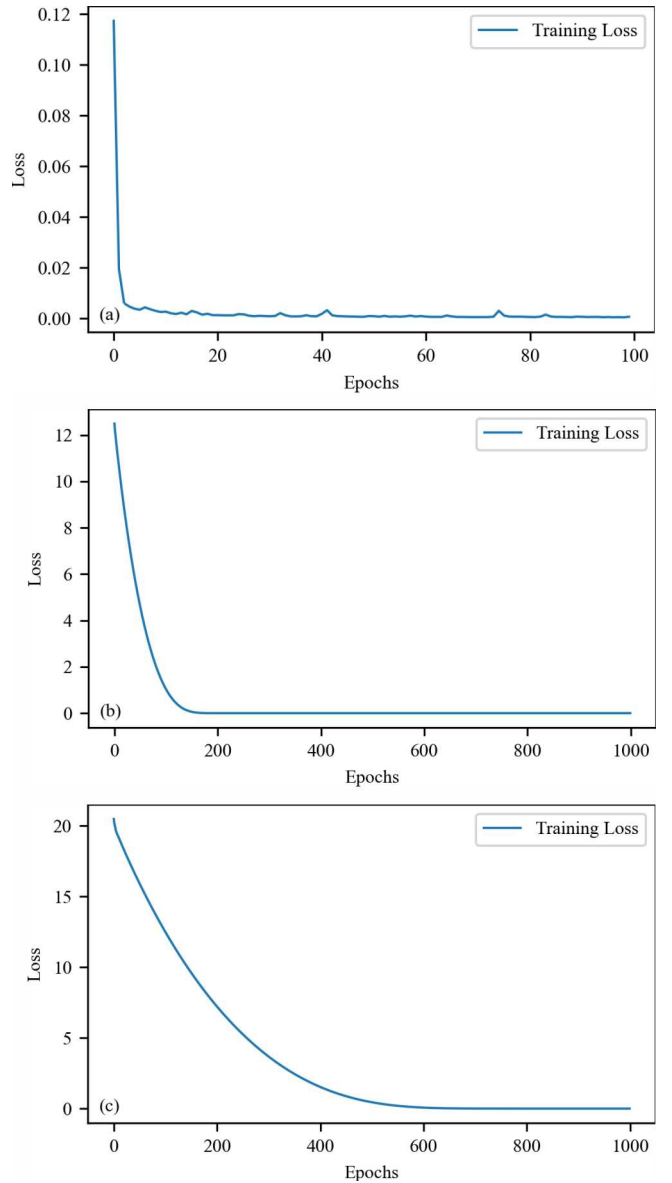


Fig. 4. Training loss curves for (a) PINN, (b) iPINN, and (c) iBPINN in inversion of Marmousi2 synthetic seismic data as a function of training epochs.

stabilizing after about 200 epochs. This is because iPINN needs to jointly optimize both the subsurface physical parameters and the wavelet frequency, increasing the dimensionality and complexity of the parameter space. Overall, iPINN is still able to achieve a comparably low loss value under unknown frequency conditions, reflecting its adaptability to frequency uncertainty.

For iBPINN [see Fig. 4(c)], Bayesian inference and KL divergence regularization are further incorporated into the network structure, resulting in a loss curve that decreases more slowly and continuously, with a convergence rate lower than those of the other two methods and stabilizing at around 600 epochs. This is mainly due to the fact that iBPINN needs to jointly optimize both the means and uncertainties of the physical parameters, and the KL divergence regularization imposes a strong constraint on the weight distribution, especially in the early stages of training. Although iBPINN does

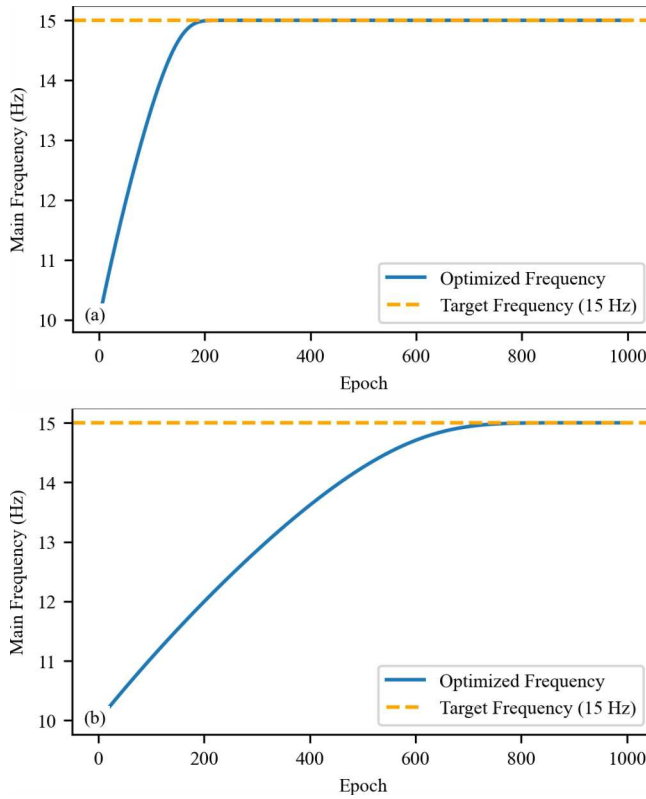


Fig. 5. Frequency optimization curves of (a) iPINN and (b) iBPINN in Marmousi2 synthetic data inversion.

not have an advantage in terms of loss convergence speed, it is capable of outputting parameter-uncertainty information, which provides a useful supplement for credibility analysis and risk assessment.

Overall, the three methods exhibit different characteristics in terms of training loss convergence and final stability: PINN converges the fastest when the wavelet frequency is known, making it suitable for rapid estimation of large-scale subsurface structures; iPINN demonstrates frequency adaptability under unknown or mismatched wavelet conditions; and iBPINN highlights the advantage of uncertainty modeling, which helps to improve the interpretability and reliability of inversion results. The loss curves shown above provide the theoretical basis for subsequent comparative analyses of the inverted physical parameter distributions.

Fig. 5 presents the frequency optimization curves of iPINN [see Fig. 5(a)] and iBPINN [see Fig. 5(b)] during the inversion of Marmousi2 synthetic data. In both cases, the optimization starts from an initial frequency of 10 Hz, with a target frequency of 15 Hz indicated by the dashed line. The choice of 10 Hz as the initial frequency is intentional: it is designed to test the ability of the network to adaptively correct the main frequency when there is a significant mismatch between the prior and the true frequency, a scenario that is often encountered in practical seismic inversion, where the assumed and observed frequencies may not be consistent.

As shown in the figure, iPINN rapidly increases the main frequency within the first 200 epochs and stabilizes at the target value of 15 Hz, demonstrating the strong frequency

adaptability and effective correction of the initial mismatch. In contrast, the frequency optimization process in iBPINN is more gradual, with the main frequency approaching the target after approximately 800 epochs. This slower convergence is primarily attributed to the Bayesian framework of iBPINN, which requires the joint optimization of both the mean and uncertainty of the parameters and is further regularized by the KL divergence term. This results in more conservative parameter updates, particularly in the early training stages. Nevertheless, iBPINN ultimately achieves the accurate frequency correction.

It is worth noting that in some cases, due to the effects of regularization, optimization trajectory, or sampling stochasticity, the final optimized frequency may converge slightly below the theoretical target (e.g., around 14 Hz). Such minor deviations are common in practical inversion and numerical optimization and do not materially affect the overall consistency or reliability of the inversion results. Increasing the number of training iterations, adjusting the KL weight or tuning other hyperparameters can further improve the precision of frequency convergence.

Overall, iPINN exhibits faster convergence in frequency adaptation, while iBPINN provides enhanced robustness and credibility through the Bayesian inference. Both methods are able to effectively estimate the main frequency of the wavelet, laying a solid foundation for subsequent elastic-parameter inversion and multiangle data matching.

It should be noted that, consistent with the methodology applied throughout this study, convergence is declared only when both the training loss curve and the main frequency curve have reached stable plateaus, with no further significant improvement observed upon additional training. This dual-plateau criterion ensures the robustness and reliability of all reported results in the synthetic tests.

As shown in Fig. 2(a)–(c), the Marmousi2 synthetic model exhibits complex geological features within the 5–25-km depth range, including pronounced stratified variations in velocity and density, as well as dislocated fault structures. In the corresponding inversion results of PINN [see Fig. 6(a)–(c)], the loss converges rapidly [see Fig. 4(a)] and the model effectively captures the large-scale distribution of P-wave and S-wave velocities and density. However, some contour distortions and misalignments are observed in high-gradient fault zones, and the model exhibits limited sensitivity in resolving the details of S-wave velocity and density—two parameters that are typically less sensitive in seismic inversion—resulting in visible deep-layer artifacts.

Compared with PINN, iPINN [see Fig. 6(d)–(f)] enables adaptive optimization of the wavelet frequency, which improves the depiction of fault locations and dip variations in the shallow to mid-depth ranges (approximately 5–20 km). This leads to smoother and more geologically consistent contour transitions and tends to reduce the local oscillatory artifacts within the same number of training epochs [see Fig. 4(b)]. In contrast, iBPINN [see Fig. 6(g)–(i)], based on a Bayesian Flipout structure and posterior mean prediction, further suppresses minor ringing artifacts in both shallow and deep regions and exhibits enhanced contour

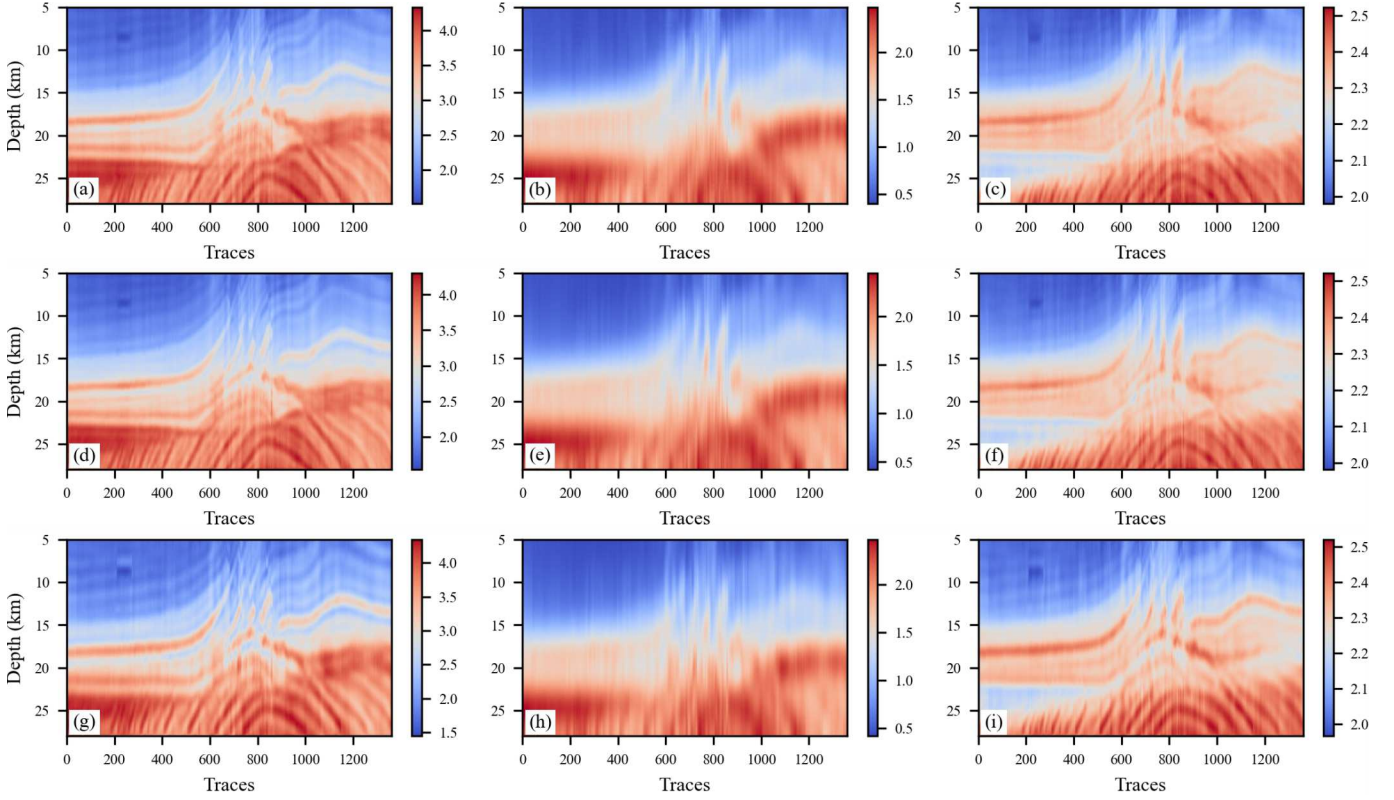


Fig. 6. Comparison of prestack AVO inversion results using PINN, iPINN, and iBPINN. (a) P-wave velocity from PINN inversion. (b) S-wave velocity from PINN inversion. (c) Density from PINN inversion. (d) P-wave velocity from iPINN inversion. (e) S-wave velocity from iPINN inversion. (f) Density from iPINN inversion. (g) P-wave velocity from iBPINN posterior mean. (h) S-wave velocity from the iBPINN posterior mean. (i) Density from the iBPINN posterior mean.

coherence and structural smoothness [see Fig. 4(c)]. Overall, the three methods each demonstrate different strengths in terms of training efficiency, reconstruction of stratigraphic structures, and detail preservation in high-gradient zones. PINN is suitable for fast estimation of large-scale velocity fields; iPINN provides additional benefits in frequency adaptivity and improved imaging in shallow and intermediate layers, while iBPINN offers enhanced profile smoothness and stability, as well as parameter-uncertainty quantification. These features make iBPINN a robust option for seismic inversion in complex geological settings or cases with limited data availability.

As shown in Fig. A1, the baseline linear least-square AVO inversion based on the Aki–Richards linearization presents clear limitations in both implementations. Implementation-1 [see Fig. A1(a)–(c)] recovers only the large-scale layering of P-wave velocity, with very limited resolution for S-wave velocity and density, and is prone to misalignments around fault zones accompanied by strong striping artifacts. Implementation-2 [see Fig. A1(d)–(f)], which incorporates combined Tikhonov regularization, wavelet prewhitening, and mild lateral smoothing, improves numerical stability and reduces striping. However, the imaging of S-wave velocity and density remains suboptimal, and deep-layer details are still poorly resolved. In comparison, the PINN, iPINN, and iBPINN frameworks (see Fig. 6) demonstrate more consistent structural continuity and greater robustness to noise, offering

complementary advantages over conventional algebraic inversion methods.

In summary, the proposed PINN, iPINN, and iBPINN frameworks each provide methodological features that supplement and, in some aspects, improve upon conventional least-squares AVO inversion. By embedding the forward wave equation into the network, PINN reformulates the problem as an end-to-end optimization process, avoiding the ill-conditioned matrix inversion inherent in algebraic approaches. The framework requires only a few global hyperparameters (e.g., learning rate and regularization weights), facilitating reproducibility across different datasets. Most importantly, the physical consistency is directly enforced through the loss function, rather than being imposed via case-specific external regularization. The capability of iBPINN to provide the uncertainty quantification further enhances the interpretability and credibility of the inversion results. The baseline least-squares results (see Fig. A1) further highlight these differences, illustrating the respective strengths and limitations of algebraic versus PINN-based inversion methods.

Fig. 7 presents the spatial distribution of the std of residuals for the inverted V_P , V_S , and ρ in the Marmousi2 synthetic data experiment. This metric reflects the fitting errors and spatial stability of each parameter across the entire model.

As shown, the STDs for all three parameters remain generally low throughout most of the model, indicating the satisfactory data-fitting performance of the inversion framework

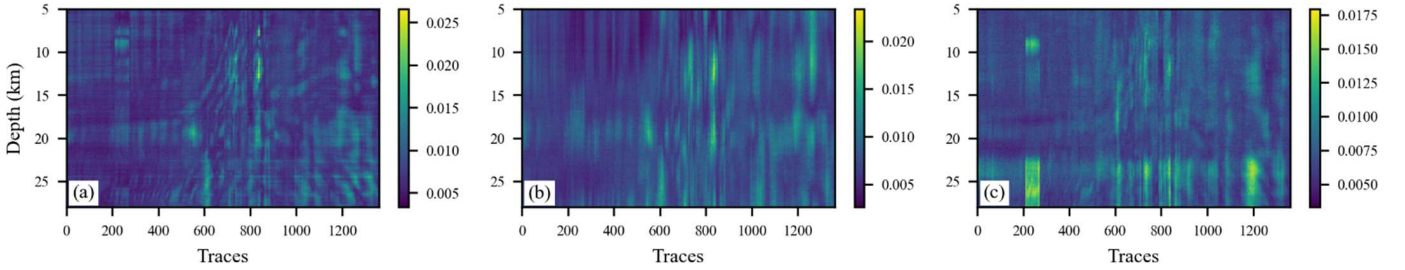


Fig. 7. STD of residuals for (a) V_P , (b) V_S , and (c) ρ .

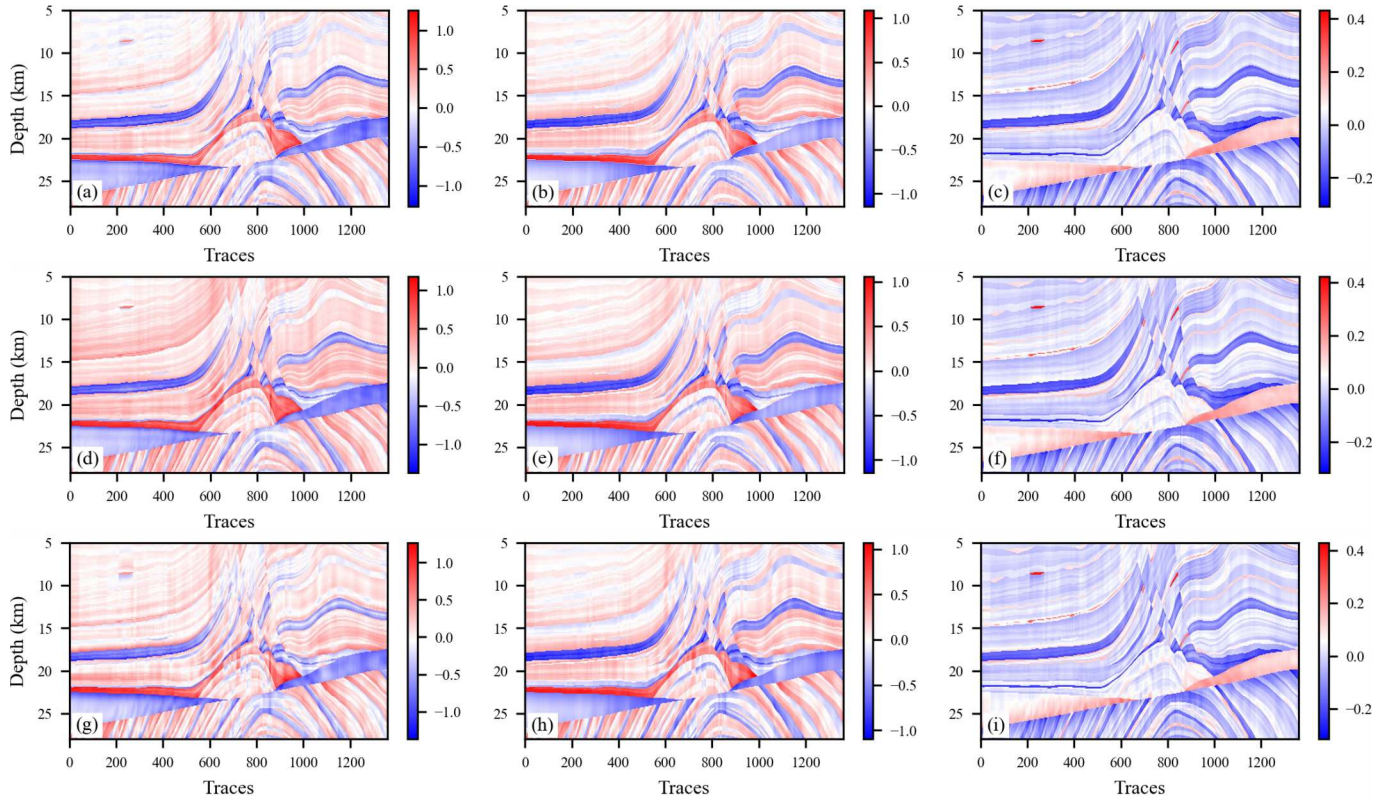


Fig. 8. Comparison of differences between inverted results and ground truth using different methods. (a) PINN: V_P difference. (b) PINN: V_S difference. (c) PINN: ρ difference. (d) iPENN: V_P difference. (e) iPENN: V_S difference. (f) iPENN: ρ difference. (g) iBPENN: V_P difference. (h) iBPENN: V_S difference. (i) iBPENN: ρ difference.

on a global scale. For V_P [see Fig. 7(a)], the std distribution is the most uniform, with most regions exhibiting values below 0.015, suggesting that the inversion errors for P-wave velocity are relatively minor and spatially consistent. Only slight increases are observed near local high-gradient fault zones. In contrast, the std maps for V_S [see Fig. 7(b)] and ρ [see Fig. 7(c)] display more heterogeneity, with localized bands or patches of higher std appearing in deeper layers and near faults. This indicates that S-wave velocity and density are more challenging to fit accurately in structurally complex regions, with greater fluctuations in spatial errors. Such behavior is consistent with the physical property that V_S and ρ are less sensitive to seismic response and often have lower signal-to-noise ratios (SNRs) in AVO inversion.

Overall, the std maps in Fig. 7 provide a direct and quantitative visualization of the inversion errors for different elastic parameters across various geological settings, facilitating an

objective assessment of model stability and reliability in complex geological environments. These metrics also serve as an important basis for further uncertainty analysis and model improvement.

Fig. 8 shows the comparison of the spatial distribution of differences between the inversion results and the ground truth obtained by different methods. All three approaches—PINN, iPENN, and iBPENN—are able to achieve reasonable reconstruction of key physical parameters in the main geological structures, though local discrepancies remain. Specifically, PINN [see Fig. 8(a)–(c)] exhibits pronounced striping artifacts and systematic deviations near high-gradient fault zones, shallow and deep boundaries, with the errors for V_S and ρ appearing more scattered, particularly in deeper regions. With adaptive frequency optimization, iPENN [see Fig. 8(d)–(f)] shows an overall reduction in error magnitude, especially around faults and in shallow-to-intermediate layers, where

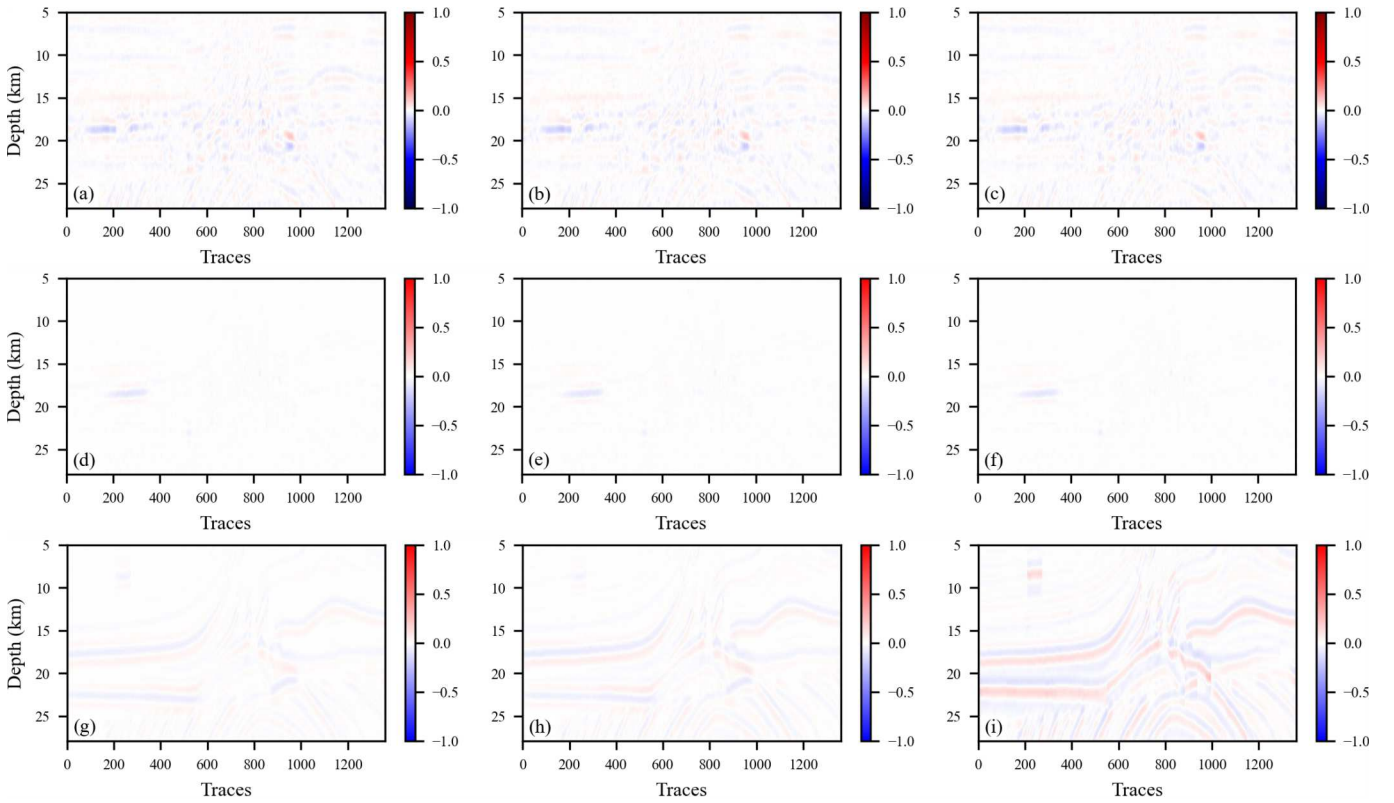


Fig. 9. Difference between synthetic gathers from inversion and real seismic data using different methods. (a)–(c) PINN: near-, mid-, and far-angle difference gathers. (d)–(f) iPENN: near-, mid-, and far-angle difference gathers. (g)–(i) iBPENN: near-, mid-, and far-angle difference gathers.

error distributions become more uniform and local anomalies are less prominent. iBPENN [see Fig. 8(g)–(i)] further suppresses errors near deep boundaries and fault zones, leading to smoother and more continuous error maps with effective mitigation of localized anomalies. Overall, while PINN tends to concentrate errors in certain regions, iPENN and iBPENN demonstrate the improved robustness in error suppression and spatial consistency.

Fig. 9 presents the different sections between the synthetic seismic gathers generated from the inversion results and real observed data for each method. PINN [see Fig. 9(a)–(c)] displays significant striping residuals across all angle gathers, with energy predominantly concentrated in shallow layers, fault zones, and most notably in far-angle gathers. The introduction of frequency adaptation in iPENN [see Fig. 9(d)–(f)] results in a marked reduction of residual amplitude, yielding a more uniform distribution, with only minor anomalies remaining in some deep fault regions. iBPENN [see Fig. 9(g)–(i)] further reduces residuals across all angles, resulting in even smoother spatial distributions. Both iPENN and iBPENN effectively mitigate errors arising from frequency mismatch, local anomalies, and observational noise, thereby improving the adaptability and generalization of the model to seismic data.

Furthermore, Fig. B1 shows the comparison of synthetic seismic gathers at near, mid, and far angles generated from the inversion results of different methods. While PINN [see Fig. B1(a)–(c)], iPENN [see Fig. B1(d)–(f)], and iBPENN [see Fig. B1(g)–(i)] all produce synthetic gathers that capture the

major waveform features in primary geological regions, iPENN and iBPENN demonstrate the enhanced lateral consistency and clearer alignment with geological structures, especially in high-gradient and deep boundary areas. Notably, iBPENN produces the smoothest gathers overall, reflecting the benefit of Bayesian modeling for waveform stability in complex scenarios.

In summary, all three PINN-based methods are capable of effective inversion for complex geological structures. However, iPENN and iBPENN exhibit higher robustness and reliability in terms of local error suppression, seismic response fitting, spatial consistency, and physical plausibility of generated gathers. These advantages provide a solid foundation for subsequent credibility assessment and uncertainty modeling in practical seismic data applications.

Fig. 10 presents the scatter plots of predicted versus true values for all elastic parameters in the testing set, together with uncertainty visualization for the iBPENN results. As shown in Fig. 10(a)–(c), the predictions from PINN, iPENN, and iBPENN all align closely with the ideal fit line ($y = x$), with coefficients of determination (R^2) of 0.91, 0.91, and 0.90, respectively. This indicates that all three methods achieve comparable overall fitting accuracy and are able to recover the main distribution characteristics of the elastic parameters without significant systematic bias or major outliers.

It is noteworthy that while iBPENN does not show a clear advantage in terms of pointwise accuracy or R^2 compared with PINN and iPENN, its primary contribution lies in providing quantitative uncertainty estimates for each prediction.

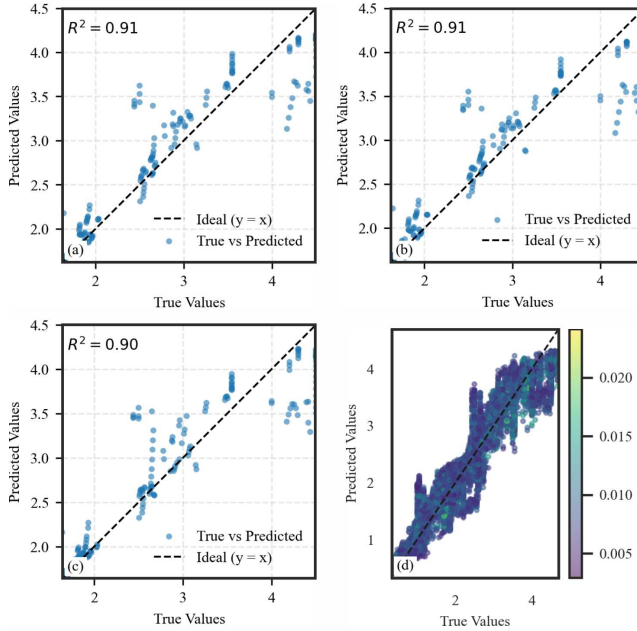


Fig. 10. Scatter plots of predicted versus true values for different methods. (a) PINN, (b) iPINN, (c) iBPINN, and (d) iBPINN with the colormap indicating prediction error magnitude.

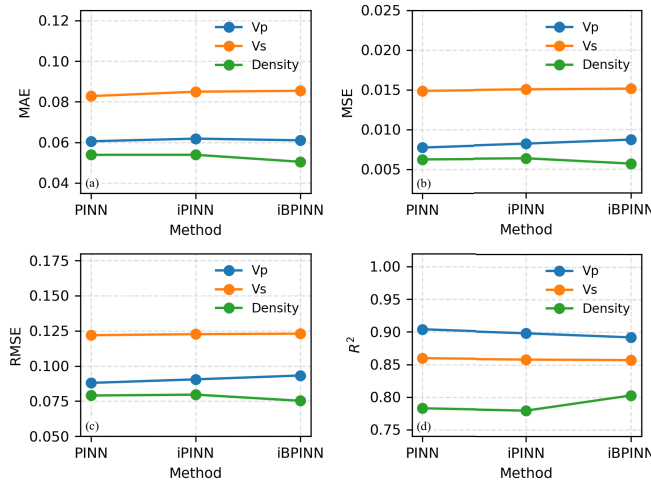


Fig. 11. Quantitative comparison of inversion accuracy among PINN, iPINN, and iBPINN for V_p , V_s , and density. (a) MAE. (b) MSE. (c) RMSE. (d) Coefficient of determination (R^2).

As illustrated in Fig. 10(d), where the scatter points are color-coded by uncertainty magnitude, the model's predictive risk distribution across different parameter ranges is clearly visualized. Regions with higher uncertainty often correspond to abrupt geological changes, areas with sparse data coverage, or locations, where the model's representation capacity is limited. This information is critical for reliability assessment and risk analysis in practical applications.

In summary, Fig. 10 not only offers a comprehensive quantitative evaluation of the global fitting accuracy for each method but also highlights the unique value of iBPINN in uncertainty quantification and credibility assessment. Such

capability is highly valuable for practical seismic inversion and result interpretation.

Fig. 11 shows a quantitative evaluation of inversion accuracy for V_p , V_s , and density using four commonly used metrics: mean absolute error (MAE), mse, RMSE, and coefficient of determination (R^2). As shown, PINN, iPINN, and iBPINN all achieve comparable performance across these accuracy metrics, with only minor differences in the error values for each parameter. This indicates that all three methods deliver consistent and reliable inversion results under the current data and experimental setup.

It is noteworthy that although iPINN and iBPINN do not exhibit significant advantages over PINN in terms of global accuracy metrics (such as MAE, mse, RMSE, and R^2), their main value lies in the extension of methodological mechanisms. By treating the wavelet frequency as a trainable parameter, iPINN enables the adaptive frequency optimization during inversion, which greatly enhances the robustness and applicability of the framework in scenarios, where the true frequency is unknown or subject to mismatch. Building upon this, iBPINN further introduces the uncertainty quantification, providing credibility estimates for each prediction. This is particularly valuable for risk assessment and exploring solution space in practical applications.

In summary, Fig. 11 not only presents a comprehensive quantitative comparison of inversion performance among different methods but also highlights the potential application value of iPINN and iBPINN in terms of physical adaptivity, generalization capability, and credibility modeling. These advantages are of great significance for addressing uncertainty in complex geological settings and real-world engineering applications.

Fig. 12 presents the iBPINN posterior mean profiles and 95% credible intervals for V_p , V_s , and ρ at trace 200, together with the initial model and the ground-truth profiles for comparison. As shown, the iBPINN posterior mean (dark blue solid line) closely tracks the major layer boundaries and structural changes of the ground truth (black dashed line), particularly at locations of sharp geological interfaces. The inferred profiles exhibit much better agreement with the true model than the initial model (orange dashed-dotted line), which is noticeably smoother and less accurate in capturing abrupt parameter variations.

A notable feature is that iBPINN provides a 95% credible interval (blue shaded band) for each depth point, directly visualizing the uncertainty associated with the inversion result. In most regions within the geological layers, the credible intervals are relatively narrow, indicating high confidence in the predicted parameters. In contrast, near fault zones and major interfaces where parameter changes are abrupt, the credible intervals become significantly wider, reflecting higher inversion uncertainty in these structurally complex regions. Such uncertainty quantification is highly valuable for subsequent geological interpretation, engineering risk assessment, and optimization of inversion strategies.

Overall, Fig. 12 not only demonstrates the satisfactory inversion accuracy of iBPINN but also highlights its advantage in providing uncertainty modeling and credibility analysis,

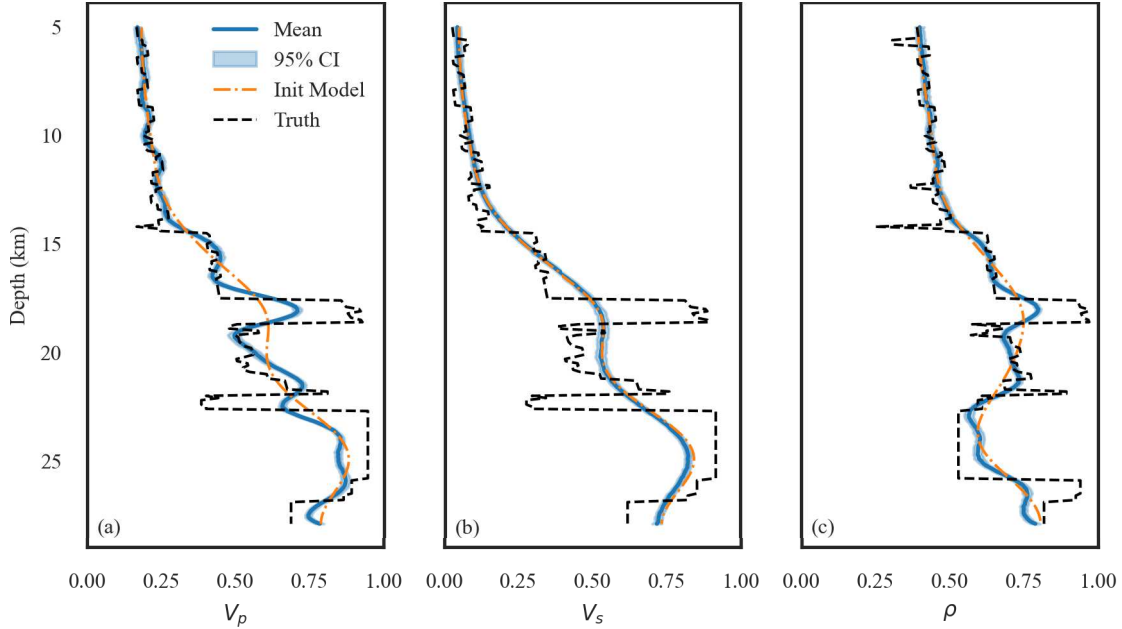


Fig. 12. iBPINN posterior mean and 95% credible interval profiles at trace 200. (a) V_p . (b) V_s . (c) ρ .

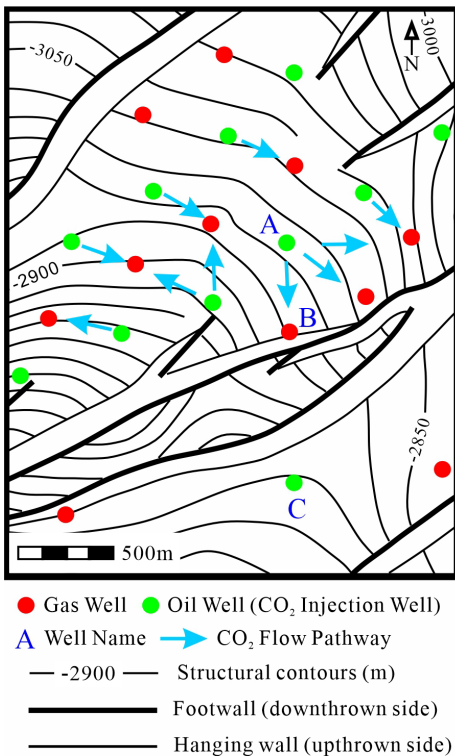


Fig. 13. Distribution map of mainstream directions of CO₂ flooding in the study area.

which supports more reliable and risk-aware subsurface characterization in practical seismic inversion.

IV. VALIDATION WITH REAL DATA

A. Overview of the Study Area

This study focuses on the X work area (see Fig. 13), which is structurally located in the central part of the Jinjia-

Zhenglizhuang-Fanjia nose-shaped structural belt within the Boxing Sag of the Dongying depression. This structural belt is a composite oil and gas accumulation zone characterized by multiple oil-bearing strata and various types of oil and gas reservoirs. It provides favorable conditions for hydrocarbon enrichment, making it an important geological background for studying CO₂ flooding technology.

The boxing sag is situated in the western part of the Dongying depression and is classified as a secondary sag. It is bounded by the Gaoqing fault to the west, adjacent to the Qingcheng Uplift, and by the Chunhua Structure to the east, separating it from the eastern part of the Dongying Depression. To the south, it connects to the Luxi Uplift; while to the north, it links to the Lijin Sag. Structurally, the sag exhibits a northwest-trending faulted and southeast-overlapping asymmetrical half-graben configuration, with a steep northwest slope and a gentle southeast slope. The development of sedimentation and tectonics in the sag is controlled by the activity of the Shicun and Gaoqing Faults. During the early Paleogene, the subsidence center was located in the hanging wall of the Shicun Fault; while in the later stages, it migrated to the Gaoqing area in the western part of the sag.

The Jinjia-Fanjia nose-shaped structural belt in the central part of the sag is a persistent structure that extends from south to north, dividing the sag into eastern and western parts. It plays a critical role in the sedimentary system and hydrocarbon accumulation.

Well log data indicate that the stratigraphy of the study area, from top to bottom, comprises the Quaternary Pingyuan Formation of the Cenozoic, the Neogene Minghuazhen and Guantao Formations, and the Paleogene Dongying, Shahejie, and Kongdian Formations. The Shahejie Formation is further subdivided into four members (Sha 1–Sha 4). The Sha 4 member exhibits an upward evolution from red mudstone interbedded with sandstone to gray mudstone, thin sandstone,

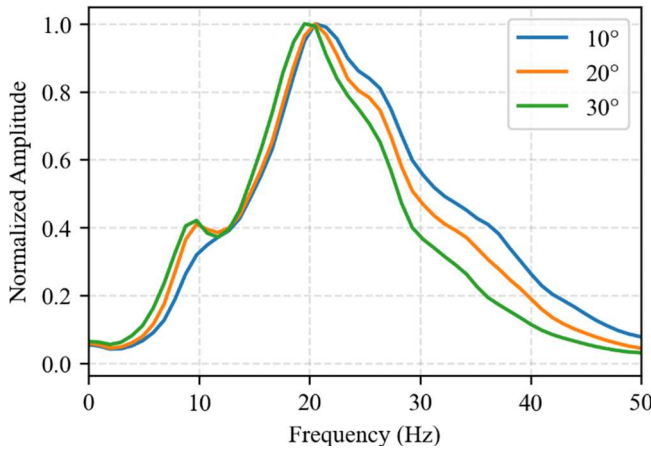


Fig. 14. Amplitude spectrum analysis of field seismic data by angle.

marl, and oil shale, reflecting a depositional transition from an arid lakeshore alluvial plain to a shallow lake and semideep lake environment under humid climatic conditions.

The main target interval of this study is the upper submember of Sha 4 member, which can be further divided into the Pure Upper and Pure Lower subunits based on lithological and electrical characteristics.

As shown in Fig. 13, the X work area is a typical test site for CO₂ capture, utilization, and storage (CCUS) under Sinopec's Shengli Oilfield. The distribution of injection and production wells is clearly delineated, and the CO₂ flow paths predominantly follow the structural lines within the work area, supported by significant regional advantages and geological conditions. Since the initiation of CO₂ injection in 2008, the scale of injection has gradually expanded. Up to date, the cumulative injection volume has exceeded 350 000 m³, and the total oil production has surpassed 330 000 tons. This not only significantly enhanced recovery rates but also achieved substantial economic and environmental benefits, providing valuable insights for the development and environmental protection of similar oilfields.

The amplitude spectrum analysis of the field seismic data at different angles is shown in Fig. 14. The results indicate that the dominant frequencies of the near (10°), mid (20°), and far (30°) angle gathers are all centered around 20 Hz, with minor variations among different angles. The spectral curves exhibit relatively consistent shapes and bandwidths, confirming that the field seismic data possess sufficient frequency content for AVO inversion across all angles. Based on this spectral analysis, the initial frequency in the inversion experiments is set to 15 Hz, while the target frequency is set to 20 Hz to match the observed dominant frequency in the field data. The presence of a clear and stable dominant frequency in all gathers ensures that the inversion framework can be effectively applied to the field data, supporting the accurate characterization of reservoir properties and monitoring of CO₂ flooding processes.

B. Inversion Performance

Figs. 15 and 16 illustrate the evolution of training loss with respect to epochs for PINN, iPINN, and iBPINN in the

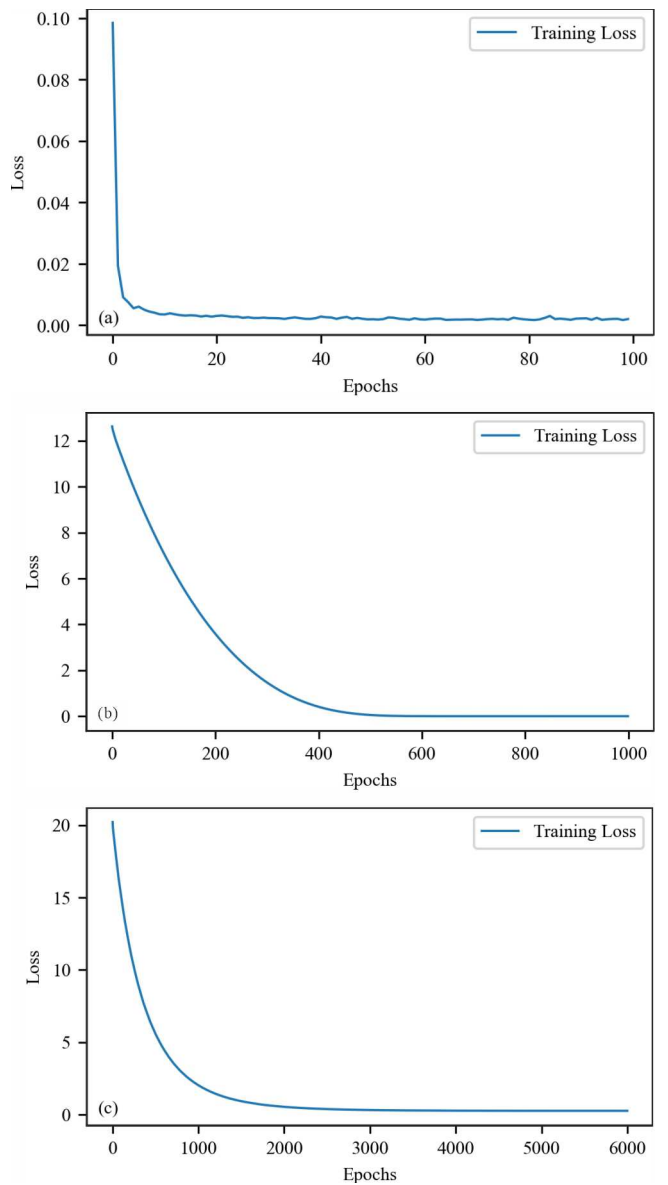


Fig. 15. Training loss curves for (a) PINN, (b) iPINN, and (c) iBPINN in inversion of field seismic data as a function of training epochs.

inversion of field seismic data, as well as the main frequency optimization processes for iPINN and iBPINN, respectively. To ensure both sufficient convergence of training and physical consistency of the results, the dual-plateau convergence criterion described earlier is adopted: the model is considered fully converged only when the training loss curve and the optimized main frequency curve simultaneously reach stable plateaus, and further training yields no significant improvement.

As shown in Fig. 15, the training losses for all three methods decrease progressively with training and eventually enter plateau regions. Specifically, PINN exhibits a rapid loss reduction within the first few dozen epochs and then quickly stabilizes, achieving convergence within 100 epochs. The loss remains nearly constant during the last 50 epochs, clearly indicating the presence of a plateau. For iPINN, the loss reaches a stable plateau after approximately 800–1000 epochs, with no obvious improvement upon continued training; thus,

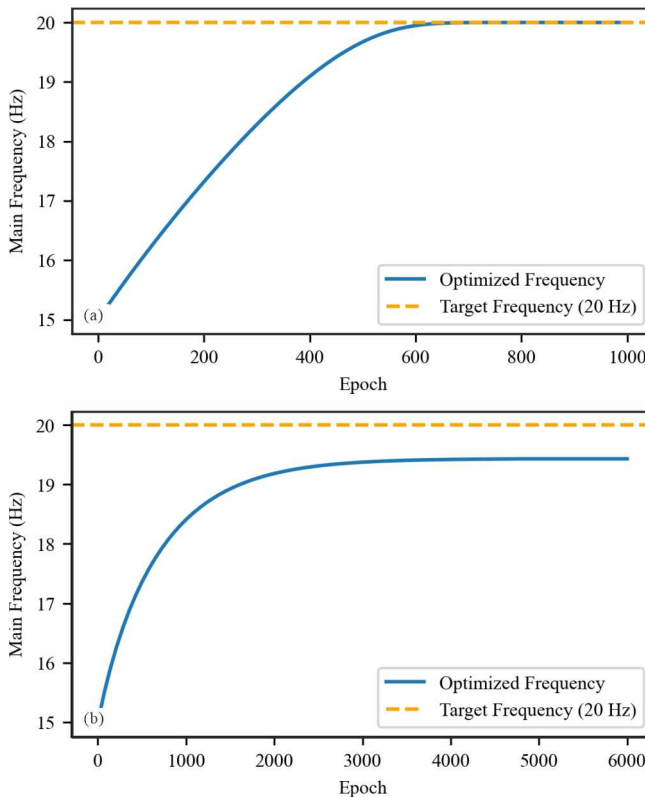


Fig. 16. Frequency optimization curves of iPINN and iBPINN in field seismic data inversion. (a) Frequency optimization curve of iPINN. (b) Frequency optimization curve of iBPINN.

1000 epochs can be regarded as sufficient for convergence. In the case of iBPINN, due to the incorporation of Bayesian uncertainty modeling and KL-divergence regularization, the loss decreases more gradually and forms a clear plateau between approximately 4000 and 6000 epochs, with the most stable convergence achieved at 6000 epochs.

Fig. 16 further demonstrates that the main frequency curves for iPINN and iBPINN also enter stable plateau regions in the later stages of training, synchronized with the loss curves. For iPINN, the main frequency rapidly converges to 20 Hz around 800–1000 epochs, consistent with the loss plateau. For iBPINN, the main frequency reaches a plateau at approximately 4000–5000 epochs and ultimately stabilizes at 19.43 Hz. It should be noted that the final frequency of iBPINN does not exactly match 20 Hz; this is the result of the combined effects of Bayesian regularization and the non-stationary characteristics of the real field wavelet, representing a robust tradeoff between the data fitting and uncertainty modeling. Such minor deviations in the main frequency are common and reasonable in seismic inversion applications.

All experiments in this study were conducted on the same CPU-only platform (AMD Ryzen 5 5500 CPU, 48-GB RAM). The training time for iPINN (1000 epochs) was 2019.54 s, while that for iBPINN (6000 epochs) was 20555.45 s, indicating that full convergence of iBPINN requires approximately ten times the computational cost of iPINN. It is worth mentioning that, for further evaluation, iBPINN was also assessed at 1000 epochs. Although the early stopped iBPINN could still produce geologically reasonable elastic parameter distributions

and physically consistent synthetic gathers, its loss and main frequency curves had not yet reached simultaneous plateaus, and the uncertainty exhibited higher variance and local fluctuations. Therefore, only results obtained when both the loss and main frequency curves reach stable plateaus are adopted as fully converged and reported in this study.

In summary, Figs. 15 and 16 collectively demonstrate that PINN, iPINN, and iBPINN all achieve dual-plateau convergence of both loss and main frequency in the inversion of field seismic data, ensuring the numerical stability and physical consistency of the inversion results. The iPINN scheme achieves a good balance between efficiency and accuracy at around 1000 epochs, while iBPINN requires longer training (with a plateau region around 4000–6000 epochs) to obtain more robust uncertainty modeling and physical interpretability. The main frequency of iBPINN ultimately stabilizes at 19.43 Hz with no systematic drift, indicating physical plausibility and model robustness. These analyses provide a solid foundation for subsequent comparative evaluation of parameter sections and uncertainty quantification.

Fig. 17 shows a comprehensive comparison of inversion results obtained from PINN, iPINN, and iBPINN for key elastic parameters and impedance attributes across the study area. The black arrows indicate the inferred CO₂ migration direction, while the black ellipses mark the target injection interval. Well logs were band-limited to match seismic bandwidth. Due to data limitations, the log curve for Well C is missing in this figure.

The horizontal subplots present the inverted property sections for P-wave velocity [see Fig. 17(a)–(c)], S-wave velocity [see Fig. 17(d)–(f)], density [see Fig. 17(g)–(i)], P-wave impedance [Z_P , Fig. 17(j)–(l)], and S-wave impedance [Z_S , Fig. 17(m)–(o)], as derived from PINN, iPINN, and iBPINN, respectively. The P-wave and S-wave impedance profiles are calculated by multiplying the predicted V_P and V_S by the predicted density (i.e., $Z_P = V_P \times \rho$ and $Z_S = V_S \times \rho$).

Within the interval between T7 and T7x, the CO₂ injection zone (highlighted in yellow) is located near Well A (the injection well). A corresponding CO₂ anomaly is also observed in the same interval near Well B, supporting the existence of subsurface connectivity between Wells A and B. By contrast, Well C exhibits no discernible CO₂ signal, confirming the absence of connectivity with the injection well. Note that due to the lack of logging data at Well C, only inversion-based profiles are shown at this location.

Comparing the inverted velocity sections, PINN [see Fig. 17(a) and (d)] exhibits generally smooth profiles near the injection zone (Traces 1700–1850), but struggles to resolve distinct low-velocity anomalies associated with CO₂ saturation. iPINN [see Fig. 17(b) and (e)] shows more pronounced low-velocity anomalies in the shallow zone (Time \approx 2000–2200 ms) and in proximity to Well A, reflecting velocity reduction due to CO₂ presence, though the continuity of such anomalies in deeper layers remains limited. In contrast, iBPINN [see Fig. 17(c) and (f)] clearly delineates a connected low-velocity anomaly between Well A and Well B, which is absent near Well C, thereby validating the migration direction and supporting the physical plausibility of the results.

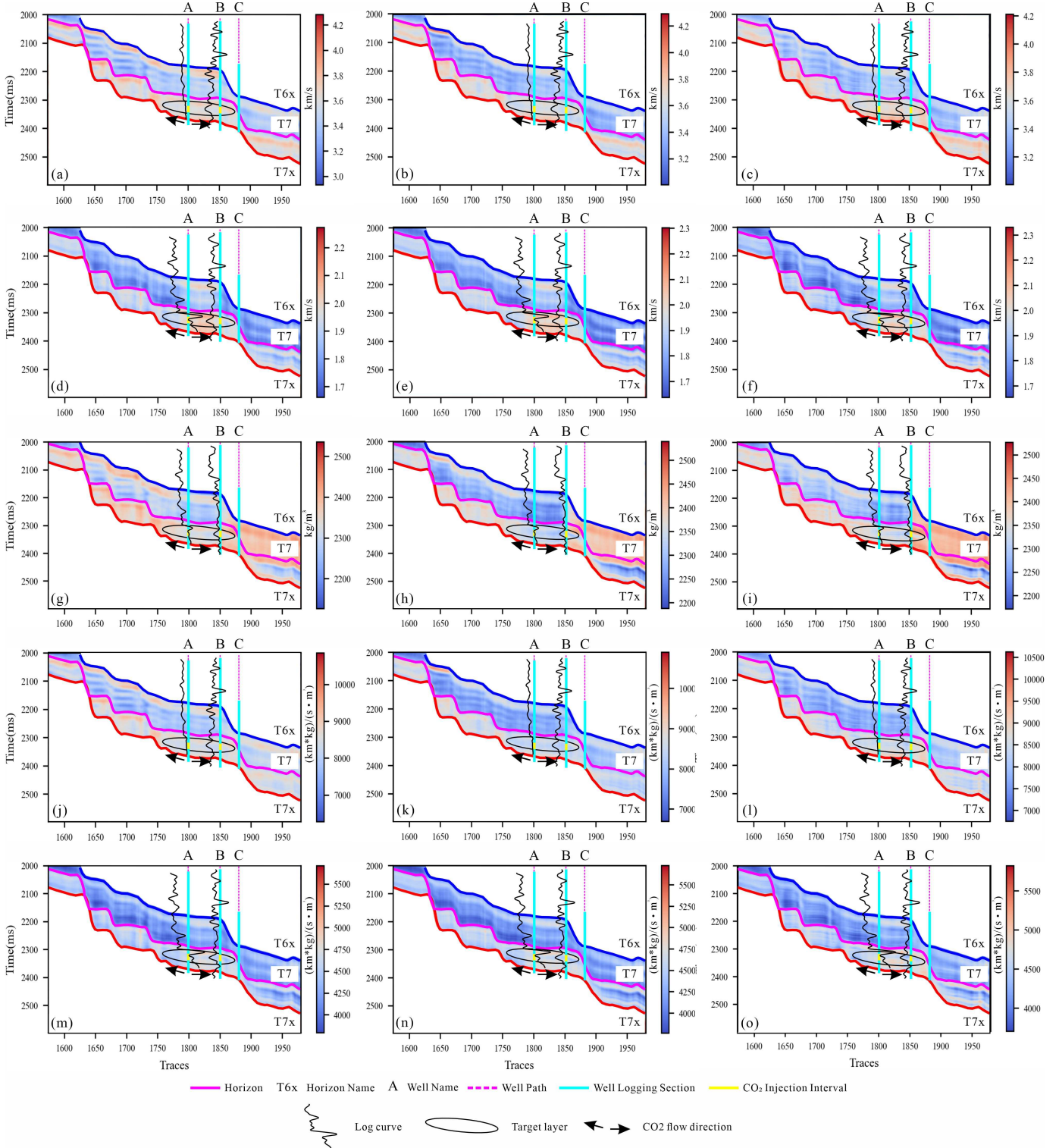


Fig. 17. Comparison of inversion results among PINN, iPINN, and iBPINN (black arrows indicate the CO₂ migration direction, and the black ellipse marks the target interval). (a) PINN: P-wave velocity. (b) iPINN: P-wave velocity. (c) iBPINN: P-wave velocity. (d) PINN: S-wave velocity. (e) iPINN: S-wave velocity. (f) iBPINN: S-wave velocity. (g) PINN: density. (h) iPINN: density. (i) iBPINN: density. (j) PINN: P-wave impedance. (k) iPINN: P-wave impedance. (l) iBPINN: P-wave impedance. (m) PINN: S-wave impedance. (n) iPINN: S-wave impedance. (o) iBPINN: S-wave impedance.

For density, PINN [see Fig. 17(g)] and iPINN [see Fig. 17(h)] display only minor localized anomalies, whereas iBPINN [see Fig. 17(i)] reveals a broader and more continuous low-density corridor between Wells A and B, consistent with

effective CO₂ displacement. The density at Well C remains at the background level.

The impedance profiles further reinforce these observations. PINN [see Fig. 17(j) and (m)] does not generate clear low-

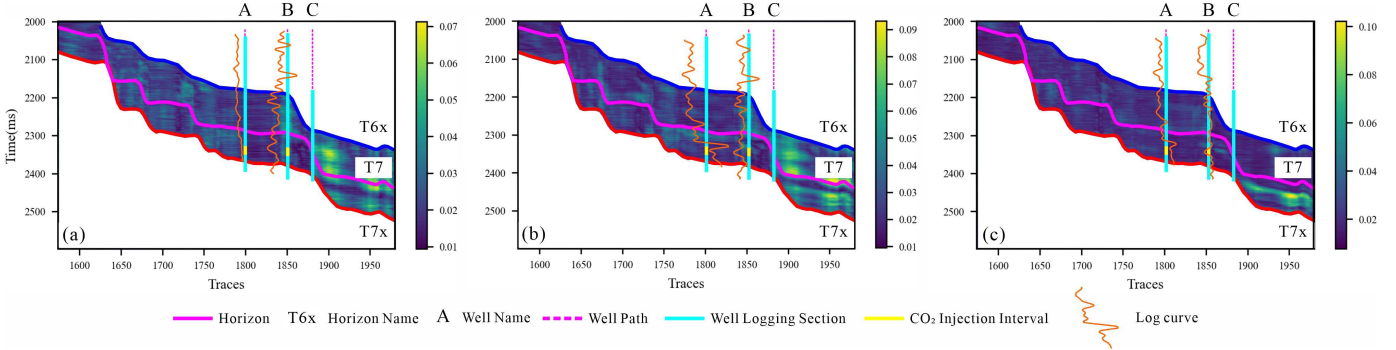


Fig. 18. STD maps of seismic residuals for iBPINN. (a) V_p std. (b) V_s std. (c) ρ std.

impedance zones, and iPINN [see Fig. 17(k) and (n)] shows limited impedance reduction in the shallow section. However, iBPINN [see Fig. 17(l) and (o)] produces a continuous low-impedance channel between the injection and detection wells, with this anomaly extending down to approximately time = 2300 ms, corresponding to the CO₂-affected interval at Well B.

In summary, the multiparameter analysis in Fig. 17 shows that iBPINN yields a physically consistent characterization of the CO₂ migration pathway in the study area. Compared with PINN and iPINN, iBPINN can delineate low-velocity, low-density, and low-impedance anomalies between the injection and detection wells, while maintaining normal responses elsewhere. This demonstrates its effectiveness in identifying subsurface fluid connectivity under complex field conditions.

Fig. 18 presents the std maps of seismic residuals for the iBPINN inversion, corresponding to V_p , V_s , and ρ , respectively. These std maps provide a quantitative assessment of the spatial distribution of inversion uncertainty and the stability of the predicted parameters.

As shown in the figure, most regions within the main horizons T6x, T7, and T7x exhibit low std values for V_p , V_s , and ρ , indicating high spatial consistency and confidence in the iBPINN inversion results. Localized increases in std are observed near Wells A and B, as well as in the interval between T7 and T7x. These higher uncertainty regions partially coincide with the interpreted CO₂-affected zone, suggesting that areas with more complex fluid substitution or seismic response may also exhibit greater inversion ambiguity. However, it should be emphasized that elevated std values primarily reflect zones of increased modeling uncertainty or data sensitivity and do not directly delineate the CO₂ migration pathway. Instead, the std maps serve as auxiliary risk indicators, highlighting areas, where inversion results should be interpreted with additional caution.

Overall, iBPINN delivers a physically reasonable and spatially resolved uncertainty characterization. The identification of localized high-uncertainty zones—some of which overlap with potential CO₂-affected areas—provides valuable supplementary information for reservoir interpretation and risk assessment. Such uncertainty quantification is critical for practical CO₂ monitoring and multiscenario analysis in oilfield applications.

TABLE I
QUANTITATIVE METRICS AND CICP FOR EACH PROPERTY AND WELL
WITHIN THE T6–T7X WINDOW

Well	Property	MAE	RMSE	CICP@1 σ	CICP@2 σ
A	V_p	3629	3653	46.88%	89.58%
A	V_s	1958	1992	63.54%	100.00%
A	ρ	121.7	132.7	53.12%	100.00%
B	V_p	3656	3660	65.62%	100.00%
B	V_s	2005	2007	100.00%	100.00%
B	ρ	176.6	181.0	19.79%	100.00%

Table I summarizes the MAE, RMSE, and credible interval coverage probability (CICP) for the main inversion parameters at each well within the T6–T7x window. MAE and RMSE reflect the fitting errors between the inversion results and the measured well log curves. As shown in the table, the MAE and RMSE values for each parameter at all wells are within a reasonable range, indicating that the model is able to satisfactorily reproduce the variations observed in the field log data.

CICP@1 σ and CICP@2 σ represent the proportions of well log data falling within the 68% and 95% credible intervals predicted by the model, respectively. For most parameters, CICP@2 σ reaches or approaches 100%, demonstrating that the predicted uncertainty intervals effectively encompass the measured well log data. In some local regions (such as the ρ parameter at Well B), the CICP@1 σ value is relatively low; however, the 2 σ interval still achieves comprehensive coverage, supporting multisolution analysis and anomaly warning for reservoir monitoring and risk assessment.

Overall, the inversion results show a high degree of agreement with the well log data, while also providing uncertainty quantification and practical value for engineering applications. These quantitative analyses offer reliable scientific support for oil and gas reservoir monitoring and CO₂ storage risk assessment under complex geological conditions.

Fig. 19 presents the difference sections between the synthetic seismic gathers generated by the PINN, iPINN, and

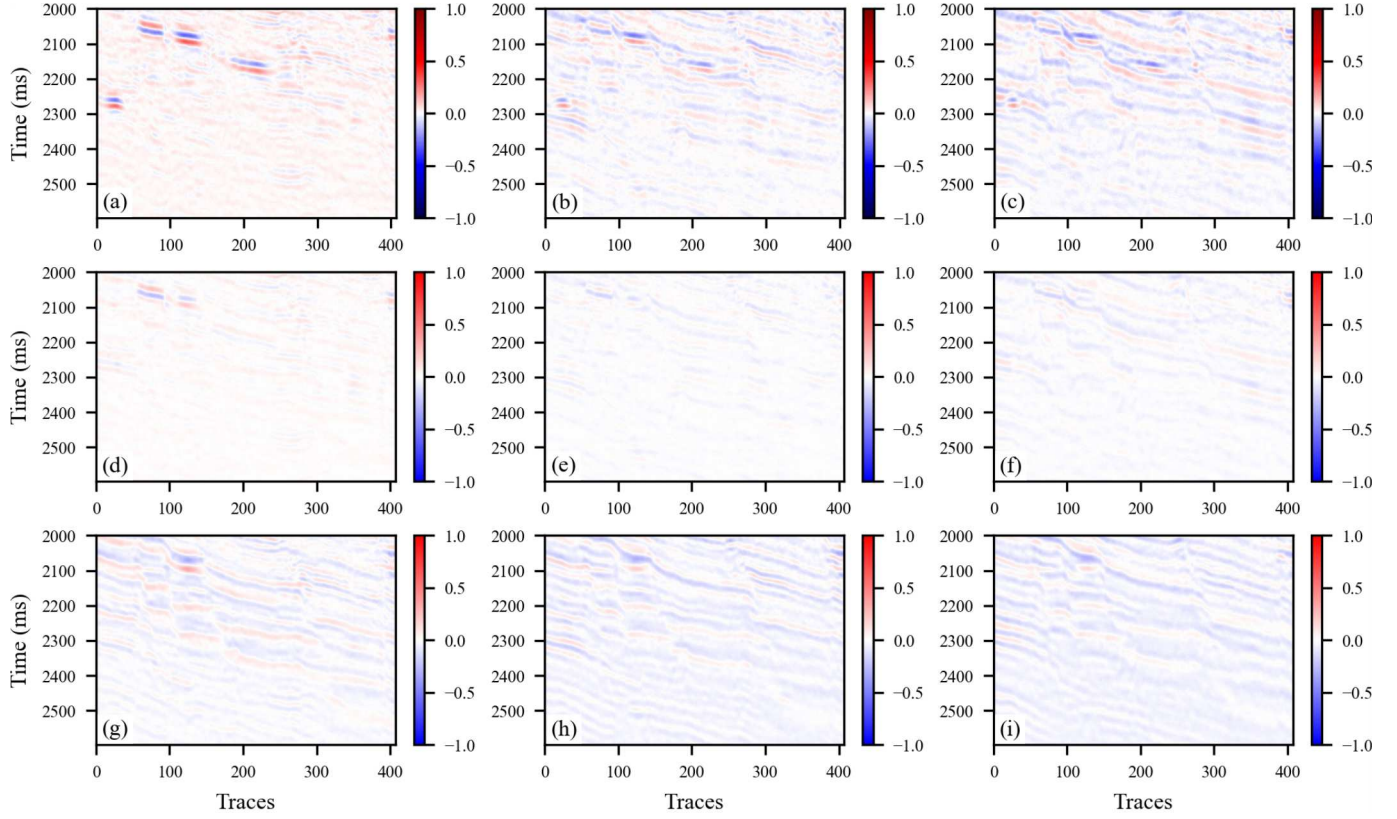


Fig. 19. Differences between synthetic and actual angle seismic data predicted by PINN, iPENN, and iBPENN. (a)–(c) PINN (near, mid, and far angles). (d)–(f) iPENN (near, mid, and far angles). (g)–(i) iBPENN (near, mid, and far angles).

iBPENN methods and the corresponding actual angle-domain seismic data. These different sections, displayed for near, mid, and far angles, provide a direct visual evaluation of the waveform-fitting capability for each method across different incident angles.

For all methods, the overall amplitude of the residuals remains relatively low, indicating a satisfactory agreement between the predicted and observed seismic waveforms. Comparing the three approaches, it is observed that iPENN and iBPENN produce residual distributions and amplitude levels that are generally similar across all angles, reflecting their comparable fitting performance. The PINN method, in contrast, shows somewhat more pronounced residuals, particularly in the deeper and higher angle (far angle) sections, which may indicate challenges in capturing subtle waveform features under more complex conditions.

The use of a frequency-adaptive mechanism in iPENN contributes to localized reductions in residual amplitude in certain areas. However, the introduction of Bayesian modeling in iBPENN does not lead to a significant further reduction in residuals compared to iPENN; instead, its primary contribution lies in the ability to output spatially resolved parameter-uncertainty estimates, supporting the subsequent reliability assessment and multisolution interpretation in practical seismic inversion scenarios.

Overall, these different sections demonstrate that all three methods achieve reasonable waveform consistency with the field seismic data, while iPENN and iBPENN offer additional

capabilities in frequency adaptation and uncertainty quantification, respectively.

Fig. B2 presents a direct comparison between the synthetic seismic data predicted by the PINN, iPENN, and iBPENN methods and the corresponding actual angle-domain seismic data, across near, mid, and far offsets. The panels in each row display the predicted synthetic gathers for each method, enabling a visual evaluation of the waveform consistency and event alignment between the predicted and observed seismic responses.

Overall, the synthetic gathers generated by all three methods demonstrate a high degree of similarity with the actual seismic data, as evidenced by the clear alignment of reflection events and the preservation of major waveform features across different angles. The PINN results [see Fig. B2(a)–(c)] accurately reproduce the main reflectors and waveform patterns but show some deviations in amplitude and subtle event mismatches, particularly at deeper times and larger offsets. The iPENN [see Fig. B2(d)–(f)] further improves the agreement in certain regions, with enhanced event continuity and amplitude consistency, which can be attributed to its frequency-adaptive inversion strategy. The iBPENN results [see Fig. B2(g)–(i)] closely match those of iPENN, maintaining strong event alignment and waveform fidelity across all angles.

In summary, the synthetic gathers predicted by all three methods show satisfactory agreement with the observed seismic data, and the additional features provided by iPENN and iBPENN—namely, frequency adaptation and uncertainty

TABLE II
FUNCTIONAL MECHANISMS AND APPLICATION HIGHLIGHTS

Method	Core Mechanism / Elements	Problem-oriented Role	Primary Outputs / Descriptors
PINN	Zoeppritz-based physics constraint and data consistency term in the loss; first- & second-order smoothness regularization; differentiable Ricker convolution	End-to-end unsupervised angle-domain inversion with emphasis on physical consistency and lateral continuity	Elastic-parameter profiles
iPINN	Trainable wavelet central frequency f_0 ; frequency constraint; joint optimization of parameters and f_0	Frequency-adaptive configuration for cases with unknown/mismatched source frequency	Elastic-parameter profiles; frequency optimization trajectory/curve
iBPINN	Flipout Bayesian layers; ELBO; KL divergence regularization with annealing	Spatially distributed parameter uncertainty and credible-interval description for interpretation and decision support	Posterior means; per-point standard deviation (std) / credible-interval maps

quantification—offer practical value for advanced seismic inversion and reservoir characterization.

V. Discussion

A. Paradigm Evolution of AI: From “Statistics” to “Logic + Reasoning”: Recent advances in AI for geophysical inversion have undergone a notable paradigm evolution—from purely statistical models to logic-embedded frameworks, and finally to reasoning-enhanced architectures. This methodological trajectory is exemplified by the progression from PINN to iPINN, and ultimately to iBPINN (see Figs. 1 and 2 and Sections II and III). PINN represents the “statistics + logic” stage, integrating physical constraints (such as the Zoeppritz equations) into deep neural networks to ensure both data-driven and physically consistent predictions. iPINN advances this concept by treating the wavelet frequency as a learnable parameter, further coupling statistical fitting with physical adaptability. iBPINN pushes the evolution further by incorporating Bayesian reasoning (e.g., Flipout layers and KL divergence), which enables not only logic-constrained inversion, but also principled uncertainty quantification (see Figs. 12 and 18). This methodological evolution mirrors broader trends in AI: from statistics, to logic, to logic + reasoning. It provides a unified framework for developing robust, interpretable, and trustworthy seismic inversion tools.

B. Inversion Accuracy and Computational Efficiency:

Through systematic tests on both synthetic and field data (Figs. 6–12, 13–19, and Fig. B2), all three methods—PINN, iPINN, and iBPINN—are shown to effectively recover the principal elastic parameters (V_P , V_S , and ρ) and impedance attributes, reproducing major stratigraphic features and fluid migration patterns (see Figs. 6 and 17). Quantitative metrics such as MAE, MSE, RMSE, and R^2 (see Fig. 11) indicate that iPINN and iBPINN achieve accuracy levels comparable to PINN for less sensitive parameters like ρ versus and ρ , while all three methods offer similar overall fitting performance. It is noteworthy that iBPINN does not consistently outperform iPINN in terms of residual amplitude or local waveform matching (see Fig. 19), but both methods yield comparable results for waveform fitting in synthetic and field datasets.

Regarding computational efficiency, PINN converges most rapidly due to the fixed frequency constraint, requiring only a few epochs to achieve stable loss values (see Figs. 4 and 15). iPINN, which jointly optimizes both frequency and physical parameters, benefits from frequency adaptation and generally converges within tens to hundreds of epochs (see Figs. 4 and 15). iBPINN, which must optimize both mean and uncertainty under Bayesian inference and KL regularization, requires more iterations to reach convergence. Each method presents distinct tradeoffs in computational cost, accuracy, and robustness, suggesting that phased or hybrid strategies could be advantageous in practical applications.

C. Effectiveness of Frequency Optimization: Frequency adaptation is a core innovation of iPINN and iBPINN, designed to address the challenge of unknown or mismatched wavelet frequencies in real-world applications (see Fig. 14). The frequency optimization curves (Figs. 5 and 16) demonstrate that iPINN can efficiently adjust the wavelet frequency from the initial value (e.g., 15 Hz) to the optimal value (e.g., 20 Hz), thereby reducing residuals and improving fits across all angles. iBPINN, owing to more conservative Bayesian regularization, may converge more gradually and occasionally stabilize at slightly lower frequencies (e.g., 19.43 Hz); this is also reflected in the residual maps (see Fig. 19). Overall, frequency adaptation significantly enhances multiangle data consistency and model adaptability.

D. Importance of Uncertainty Quantification in iBPINN

A distinct advantage of iBPINN lies in its ability to quantify parameter uncertainty, providing spatially resolved std or credible interval maps for each parameter (see Figs. 12 and 18). While iPINN and iBPINN offer similar accuracy in point estimates, only iBPINN can explicitly highlight regions of higher uncertainty—such as the main CO₂ migration pathway—thus improving the interpretability and risk analysis of inversion results. The std distributions (see Fig. 18) reveal that uncertainties are primarily concentrated in CO₂-affected zones, well vicinities, and geologically complex areas, which correlates well with data coverage and structural variation. This capability is valuable for CO₂ monitoring, well planning, and data acquisition optimization in oilfield applications.

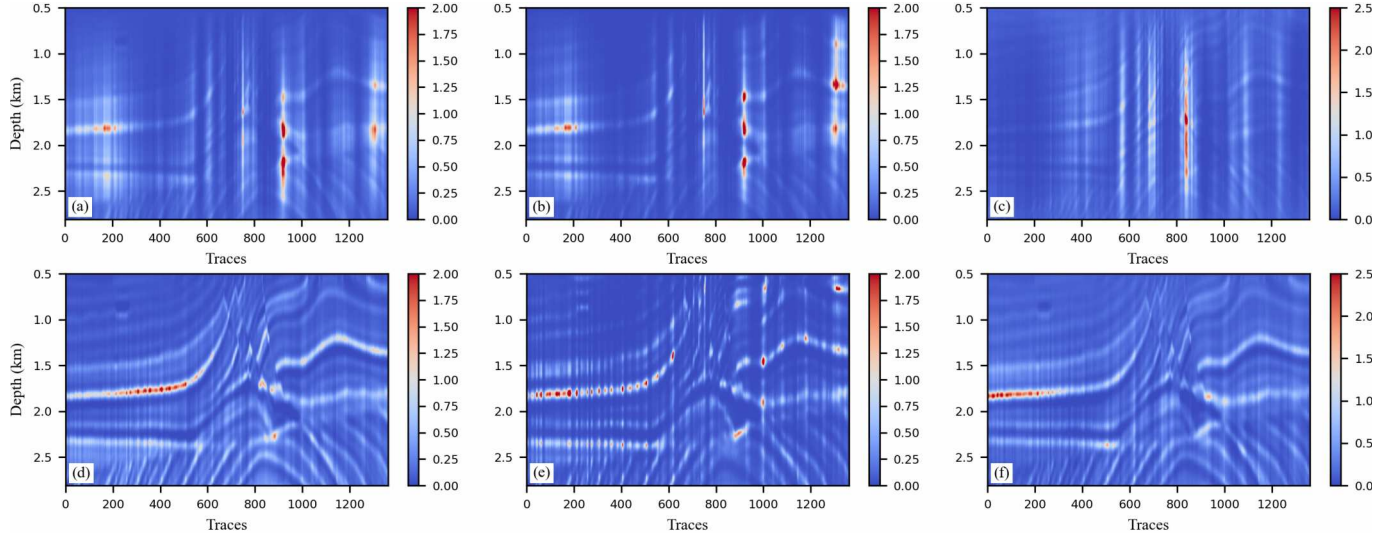


Fig. A1. Baseline linear least-squares AVO inversion (Aki–Richards): comparison of two implementations. (a)–(c) Implementation-1: V_p , V_s , and ρ . (d)–(f) Implementation-2: V_p , V_s , and ρ .

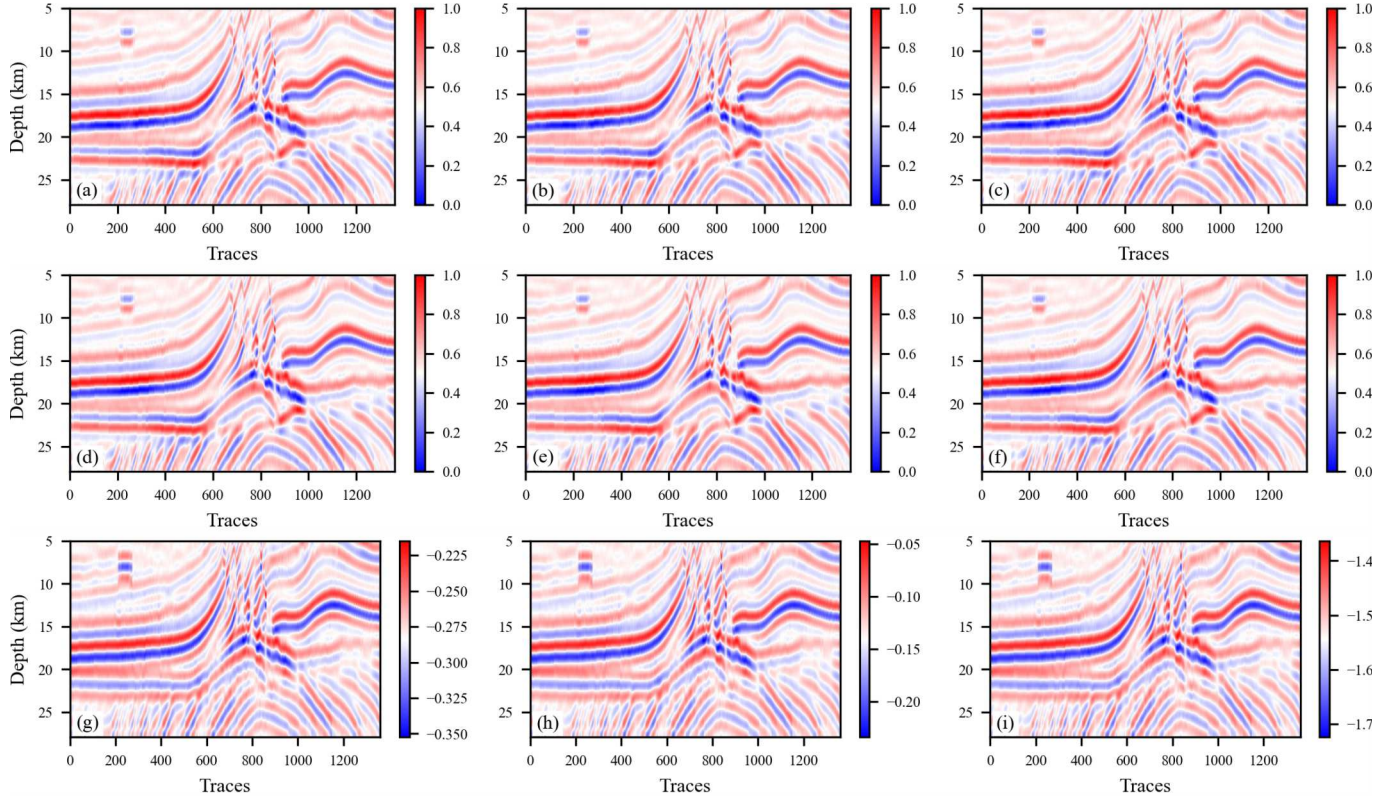


Fig. B1. Comparison of synthetic seismic gathers at different angles generated from inversion results. (a)–(c) PINN: near-, mid-, and far-angle seismic. (d)–(f) iPINN: near-, mid-, and far-angle seismic. (g)–(i) iBPINN: near-, mid-, and far-angle seismic.

E. Summary of Innovations and Highlights

To help readers grasp the methodological structure and engineering applicability of this work, we summarize the core mechanisms and functional roles of the three methods used throughout this article—PINN, iPINN, and iBPINN (see Table II).

Mechanisms: PINN embeds a Zoeppritz-based physics constraint and a data-consistency term in the loss, and employs first- and second-order smoothness regularization to balance

identifiability with lateral continuity. Building on this, iPINN treats the Ricker wavelet central frequency f_0 as a learnable parameter, adds a frequency-constraint term, and thus enables adaptive modeling of the source frequency. Furthermore, iBPINN introduces Flipout Bayesian layers and ELBO with KL-divergence regularization and annealing, producing posterior means and per-point STDs for spatially distributed parameter-uncertainty quantification.

Applications: PINN targets unsupervised angle-domain inversion with an emphasis on physical consistency; iPINN

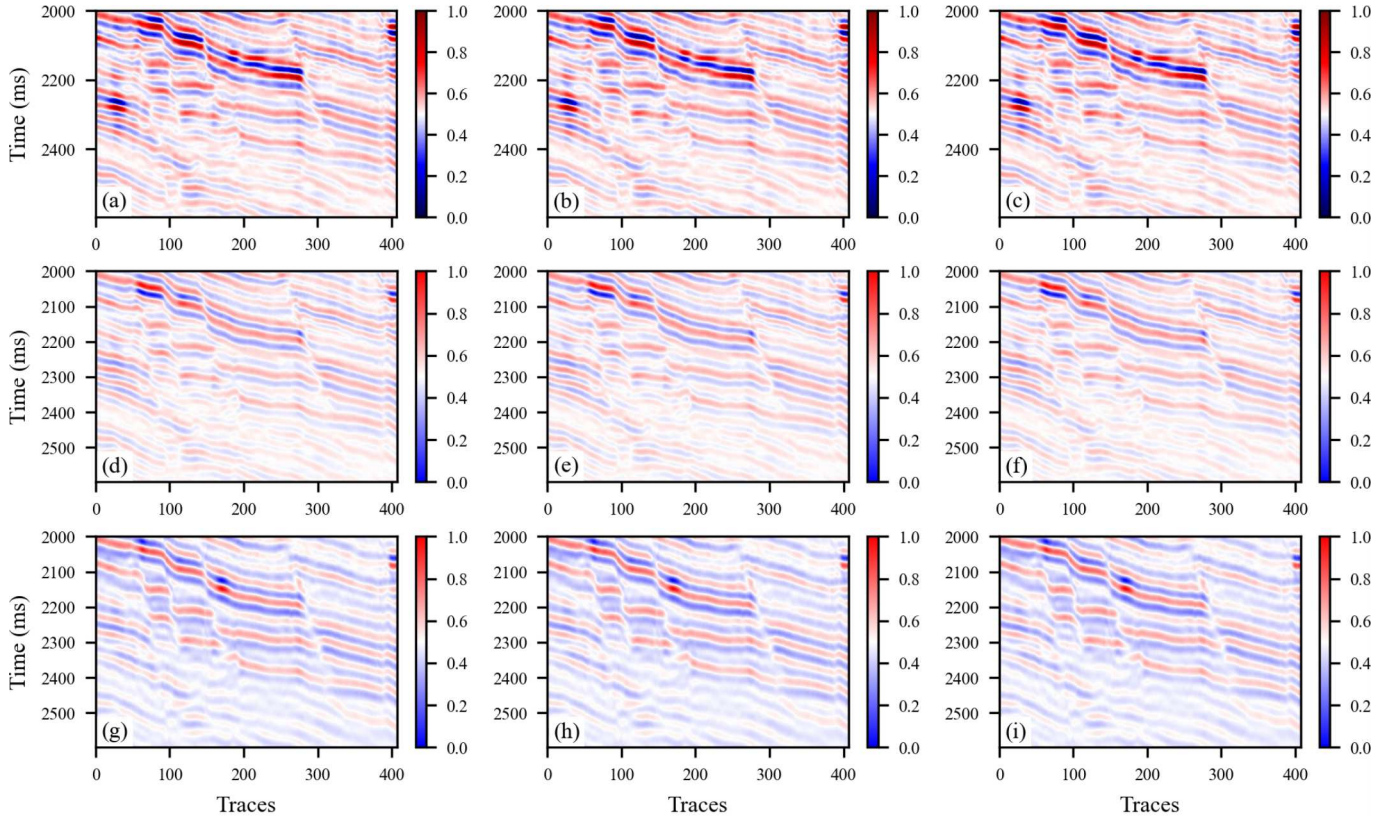


Fig. B2. Comparison of the seismic data predicted by PINN, iPINN, and iBPINN: synthetic seismic data versus actual angle seismic data. (a)–(c) Synthetic seismic data generated from PINN predictions for near, mid, and far angles, respectively. (d)–(f) Synthetic seismic data generated from iPINN predictions for near, mid, and far angles, respectively. (g)–(i) Synthetic seismic data generated from iBPINN predictions for near, mid, and far angles, respectively.

provides a frequency-adaptive configuration for cases with unknown or mismatched source frequency; iBPINN is intended for interpretation scenarios requiring per-point uncertainty representation and credible-interval description (e.g., credibility indication and risk flagging).

Paradigm Evolution: The progression PINN \rightarrow iPINN \rightarrow iBPINN reflects a “statistics–logic–reasoning” evolution that organically integrates physical constraints, frequency adaptation, and variational Bayesian uncertainty modeling within a single computation graph. This yields a reproducible, unified workflow for seismic inversion that bridges data-consistency formulation and credibility (uncertainty) quantification within the same framework.

VI. CONCLUSION

This study proposes and validates a prestack AVO inversion framework based on PINN, iPINN, and iBPINN, highlighting the paradigm evolution of AI from “statistical” to “logical + reasoning” approaches. By embedding physical constraints and uncertainty inference into data-driven models, the framework significantly enhances model interpretability and credibility.

The PINN method directly incorporates seismic forward modeling equations into the neural network loss function and introduces both first- and second-order regularization to improve the lateral continuity of inversion results. This design enables fully unsupervised inversion that adheres to physical laws even under limited data conditions, thereby promoting the physical consistency and spatial stability of

subsurface parameter predictions. Building on this, iPINN treats the wavelet central frequency as a learnable parameter, endowing the network with adaptive frequency calibration and supporting residual reduction across angles in certain regions. iBPINN further extends iPINN’s physical constraints and frequency adaptation by introducing Flipout Bayesian layers and KL divergence regularization. Through variational inference, it enables probabilistic modeling of both network weights and wavelet parameters, outputting not only the mean values of physical parameters but also their quantified uncertainties—providing valuable support for geological interpretation and risk assessment.

Experimental results on both synthetic and field data demonstrate that PINN can reliably estimate V_P with limited training samples and achieves rapid convergence. iPINN provides stable and consistent inversion behavior for weakly sensitive parameters such as V_S and ρ , and, via frequency learning, helps reduce multiangle waveform-fitting residuals in specific areas. Leveraging Bayesian inference, iBPINN produces smoother lateral distributions in high-gradient deep zones and generates std maps that highlight regions of high uncertainty, which is valuable for applications such as CO₂ migration tracking and reservoir connectivity identification.

Although the proposed framework demonstrates promising performance in 2-D scenarios, several challenges remain for large-scale 3-D applications. First, the uncertainty coverage of iBPINN is lower than theoretical expectations, which could be improved by increasing sampling, refining KL

annealing strategies, or adopting broader priors. Second, the computational and memory demands of Flipout layers and KL divergence in 3-D CNNs call for further optimization through parallelization, multiscale PINNs, or model compression techniques. Third, the current implementation treats wavelet frequency as a global learnable scalar; the future work may extend this to depth- or location-dependent parameters for more precise spectral calibration in heterogeneous formations. Finally, the model's generalization ability under cross-field transfer and few-shot fine-tuning requires further validation.

In summary, the proposed PINN-based framework integrates physical priors, data-driven learning, and Bayesian inference to establish a methodological foundation for next-generation AVO inversion with quantified uncertainty and reliability in complex geological settings. The ability of iBPINN to provide spatially resolved uncertainty quantification offers valuable support for credibility assessment and risk-based interpretation. While the framework demonstrates satisfactory results in 2-D scenarios, further developments in computational efficiency, prior modeling, and 3-D scalability will be essential for large-scale field deployment. Overall, this work contributes to advancing robust, interpretable, and trustworthy seismic inversion methods for practical applications such as carbon storage monitoring, hydrocarbon exploration, and geohazard risk assessment.

APPENDIX

A. Baseline Results

The baseline linear least-squares AVO inversion based on the Aki–Richards linearization was implemented in two forms. The results are shown in Fig. A1. Implementation-1 represents the simplest textbook version with first-order Tikhonov regularization, while Implementation-2 introduces additional stabilization measures, including wavelet prewhitening, column normalization, and composite regularization.

B. Implementation-1 (Basic)

- 1) *Design Matrix:* Toeplitz convolution matrices were constructed for each incidence angle, and combined into a block-diagonal design matrix using time-varying A–C coefficients.
- 2) *Regularization:* First-order Tikhonov regularization was applied in the time direction, with parameter weights $\lambda = [2 \times 10^{-2}, 2 \times 10^{-2}, 4 \times 10^{-2}]$, for V_P , V_S , and ρ .
- 3) *Solver:* the normal equations ($G^\top G + \text{Reg} + \varepsilon I$) $m = G^\top d$ were solved with direct inversion ($\varepsilon = 10^{-10}$), with a fallback to least-squares when singular.
- 4) *Integration:* reflectivities were integrated to V_P , V_S , and ρ using Gaussian-smoothed low-frequency trends as anchors ($\alpha = 0.1$).

This version reflects the simplest and most conventional form of least-square inversion, and serves as a strict baseline.

C. Implementation-2 (Robust)

- 1) *Preconditioning:* The Ricker wavelet was prewhitened to unit energy, and the columns of the design matrix were normalized to reduce condition numbers.

- 2) *CompositeRegularization:* Combined first- and second-order difference operators with a weak zeroth-order damping.

$$L^\top L = D_1^\top D_1 + 0.5 D_2^\top D_2 + \lambda_0 I, \lambda_0 = 10^{-3}$$

with parameter weights $\lambda = [0.4, 0.6, 1.0]$ for V_P , V_S , and ρ .

- 3) *Solver:* The normal equations were solved in the scaled domain with back-scaling afterward, including a small diagonal buffer ($\varepsilon = 10^{-6}$).
- 4) *Postprocessing:* Mild lateral Gaussian smoothing was applied to the reflectivity estimates ($\sigma \approx 0.8/1.0/1.2$ for $V_P/V_S/\rho$), suppressing stripy artifacts for display only.
- 5) *Integration:* Integration to absolute parameters used the same low-frequency anchors as in Implementation-1.

This robust version improves the numerical stability and reduces striping artifacts, but still retains the limitations of linear algebraic inversion, particularly for S-wave velocity and density.

REFERENCES

- [1] L.-Q. Yang, S.-D. Wang, and J.-M. Li, "Few-shot pre-stack AVO inversion using a multi-task Transformer," *Prog. Geophys.*, vol. 40, no. 2, pp. 743–757, Feb. 2025.
- [2] D. Grana, E. Paparozzi, S. Mancini, and C. Tarchiani, "Seismic driven probabilistic classification of reservoir facies for static reservoir modelling: A case history in the Barents Sea," *Geophys. Prospecting*, vol. 61, no. 3, pp. 613–629, May 2013, doi: [10.1111/j.1365-2478.2012.01115.x](https://doi.org/10.1111/j.1365-2478.2012.01115.x).
- [3] O. Koefoed, "On the effect of Poisson's ratios of rock strata on the reflection coefficients of plane waves," *Geophys. Prospecting*, vol. 3, no. 4, pp. 381–387, Dec. 1955.
- [4] M. Muskat and M. W. Meres, "Reflection and transmission coefficients for plane waves in elastic media," *Geophysics*, vol. 5, no. 2, pp. 115–148, Apr. 1940.
- [5] K. Aki and P. G. Richards, *Quantitative Seismology: Theory and Methods*. San Francisco, CA, USA: W. H. Freeman, 1980.
- [6] A. Buland, O. Kolbjørnsen, and H. Omre, "Rapid spatially coupled AVO inversion in the Fourier domain," *Geophysics*, vol. 68, no. 3, pp. 824–836, May 2003, doi: [10.1190/1.1581035](https://doi.org/10.1190/1.1581035).
- [7] A. Buland and H. Omre, "Bayesian linearized AVO inversion," *Geophysics*, vol. 68, no. 1, pp. 185–198, Jan. 2003.
- [8] S. E. Dosso, C. W. Holland, and M. Sambridge, "Parallel tempering for strongly nonlinear geoacoustic inversion," *J. Acoust. Soc. Amer.*, vol. 132, no. 5, pp. 3030–3040, Nov. 2012, doi: [10.1121/1.4757639](https://doi.org/10.1121/1.4757639).
- [9] B. Wang, R. Sun, X. Yin, and G. Zhang, "Nonlinear inversion based on metropolis sampling algorithm," *Oil Geophys. Prospecting*, vol. 50, no. 1, pp. 111–117, 2015, doi: [10.13810/j.cnki.issn.1000-7210.2015.01.017](https://doi.org/10.13810/j.cnki.issn.1000-7210.2015.01.017).
- [10] R. Kant, S. P. Maurya, K. H. Singh, K. S. Nisar, and A. K. Tiwari, "Qualitative and quantitative reservoir characterization using seismic inversion based on particle swarm optimization and genetic algorithm: A comparative case study," *Sci. Rep.*, vol. 14, no. 1, Sep. 2024, Art. no. 22581.
- [11] H. Yuan, S.-Y. Yuan, S. Qin, H.-Q. Wang, H.-H. Zeng, and S.-J. Yue, "Multi-well wavelet-synchronized inversion based on particle swarm optimization," *Appl. Geophys.*, vol. 21, no. 4, pp. 728–739, Aug. 2024.
- [12] M. Alfarraj and G. AlRegib, "Semisupervised sequence modeling for elastic impedance inversion," *Interpretation*, vol. 7, no. 3, pp. SE237–SE249, Aug. 2019, doi: [10.1190/int-2018-0250.1](https://doi.org/10.1190/int-2018-0250.1).
- [13] V. Das, A. Pollack, U. Wollner, and T. Mukerji, "Convolutional neural network for seismic impedance inversion," *Geophysics*, vol. 84, no. 6, pp. R869–R880, Nov. 2019.
- [14] W. Li, C. Chen, M. Zhang, H. Li, and Q. Du, "Data augmentation for hyperspectral image classification with deep CNN," *IEEE Geosci. Remote Sens. Lett.*, vol. 16, no. 4, pp. 593–597, Apr. 2019, doi: [10.1109/LGRS.2018.2878773](https://doi.org/10.1109/LGRS.2018.2878773).
- [15] Y. Huang, J. Huang, and Y. Ma, "A fast least-squares reverse time migration method using cycle-consistent generative adversarial network," *Frontiers Earth Sci.*, vol. 10, pp. 55–61, Aug. 2022.

- [16] Z. Li et al., "Research on influencing factors of deep learning in AVA inversion application," *J. China Univ. Petroleum*, vol. 48, no. 4, pp. 57–67, 2024.
- [17] X. Zhu, F. Wang, Y. Xu, and W. Zhang, "A comprehensive review of physics-guided deep learning: Advancements, challenges, and perspectives," *J. Frontiers Comput. Sci. Technol.*, vol. 19, no. 2, pp. 277–294, 2025.
- [18] M. L. Thompson and M. A. Kramer, "Modeling chemical processes using prior knowledge and neural networks," *AIChE J.*, vol. 40, no. 8, pp. 1328–1340, Aug. 1994.
- [19] M. Raissi, P. Perdikaris, and G. E. Karniadakis, "Physics informed deep learning (Part I): Data-driven solutions of nonlinear partial differential equations," 2017, *arXiv:1711.10561*.
- [20] M. Raissi, P. Perdikaris, and G. E. Karniadakis, "Physics informed deep learning (Part II): Data-driven discovery of nonlinear partial differential equations," 2017, *arXiv:1711.10566*.
- [21] L. von Rueden et al., "Informed machine learning—A taxonomy and survey of integrating prior knowledge into learning systems," *IEEE Trans. Knowl. Data Eng.*, vol. 35, no. 1, pp. 614–633, Jan. 2023, doi: [10.1109/TKDE.2021.3079836](https://doi.org/10.1109/TKDE.2021.3079836).
- [22] A. Karpatne et al., "Theory-guided data science: A new paradigm for scientific discovery from data," *IEEE Trans. Knowl. Data Eng.*, vol. 29, no. 10, pp. 2318–2331, Oct. 2017, doi: [10.1109/TKDE.2017.2720168](https://doi.org/10.1109/TKDE.2017.2720168).
- [23] G. E. Karniadakis, I. G. Kevrekidis, L. Lu, P. Perdikaris, S. Wang, and L. Yang, "Physics-informed machine learning," *Nature Rev. Phys.*, vol. 3, no. 6, pp. 422–440, May 2021, doi: [10.1038/s42254-021-00314-5](https://doi.org/10.1038/s42254-021-00314-5).
- [24] A. V. D. P. Adombi, R. Chesnaux, and M. Boucher, "Review: Theory-guided machine learning applied to hydrogeology—State of the art, opportunities and future challenges," *Hydrogeology J.*, vol. 29, no. 8, pp. 2671–2683, 2021.
- [25] M. Rasht-Behesht, C. Huber, K. Shukla, and G. E. Karniadakis, "Physics-informed neural networks(PINNs) for wave propagation and full waveform inversions," *J. Geophys. Res., Solid Earth*, vol. 127, no. 5, 2022, Art. no. e2021JB023120, doi: [10.1029/2021JB023120](https://doi.org/10.1029/2021JB023120).
- [26] C. Song, T. Alkhalifah, and U. B. Waheed, "Solving the frequency-domain acoustic VTI wave equation using physics-informed neural networks," *Geophys. J. Int.*, vol. 225, no. 2, pp. 846–859, May 2021, doi: [10.1093/gji/ggab010](https://doi.org/10.1093/gji/ggab010). [Online]. Available: https://ui.adsabs.harvard.edu/link_gateway/2021GeoJ.225..846S/
- [27] Y. Wu, H. S. Aghamiry, S. Operto, and J. Ma, "Helmholtz-equation solution in nonsmooth media by a physics-informed neural network incorporating quadratic terms and a perfectly matching layer condition," *GEOPHYSICS*, vol. 88, no. 4, pp. T185–T202, Jul. 2023, doi: [10.1190/geo2022-0479.1](https://doi.org/10.1190/geo2022-0479.1).
- [28] X. Chai et al., "Modeling multisource multifrequency acoustic wavefields by a multiscale Fourier feature physics-informed neural network with adaptive activation functions," *Geophysics*, vol. 89, no. 3, pp. T79–T94, 2024, doi: [10.1190/geo2023-0394.1](https://doi.org/10.1190/geo2023-0394.1).
- [29] U. B. Waheed, E. Haghigiat, T. Alkhalifah, C. Song, and Q. Hao, "PINNeik: Eikonal solution using physics-informed neural networks," *Comput. Geosci.*, vol. 155, Oct. 2021, Art. no. 104833, doi: [10.1016/j.cageo.2021.104833](https://doi.org/10.1016/j.cageo.2021.104833).
- [30] Y. Chen, S. A. L. de Ridder, S. Rost, Z. Guo, X. Wu, and Y. Chen, "Eikonal tomography with physics-informed neural networks: Rayleigh wave phase velocity in the northeastern margin of the Tibetan Plateau," *Geophys. Res. Lett.*, vol. 49, no. 21, 2022, Art. no. e2022GL099053, doi: [10.1029/2022GL099053](https://doi.org/10.1029/2022GL099053).
- [31] S. Grubas, A. Duchkov, and G. Loginov, "Neural Eikonal solver: Improving accuracy of physics-informed neural networks for solving Eikonal equation in case of caustics," *J. Comput. Phys.*, vol. 474, Feb. 2023, Art. no. 111789, doi: [10.1016/j.jcp.2022.111789](https://doi.org/10.1016/j.jcp.2022.111789).
- [32] L. Yang, X. Meng, and G. E. Karniadakis, "B-PINNs: Bayesian physics-informed neural networks for forward and inverse PDE problems with noisy data," *J. Comput. Phys.*, vol. 425, Jan. 2021, Art. no. 109913, doi: [10.1016/j.jcp.2020.109913](https://doi.org/10.1016/j.jcp.2020.109913).
- [33] R. Gou, Y. Zhang, X. Zhu, and J. Gao, "Bayesian physics-informed neural networks for the subsurface tomography based on the Eikonal equation," *IEEE Trans. Geosci. Remote Sens.*, vol. 61, 2023, Art. no. 4503012, doi: [10.1109/TGRS.2023.3286438](https://doi.org/10.1109/TGRS.2023.3286438).
- [34] R. Biswas, M. K. Sen, V. Das, and T. Mukerji, "Prestack and poststack inversion using a physics-guided convolutional neural network," *Interpretation*, vol. 7, no. 3, pp. SE161–SE174, Aug. 2019, doi: [10.1190/int-2018-0236.1](https://doi.org/10.1190/int-2018-0236.1).
- [35] C. Song and T. A. Alkhalifah, "Wavefield reconstruction inversion via physics-informed neural networks," *IEEE Trans. Geosci. Remote Sens.*, vol. 60, 2022, Art. no. 5908012, doi: [10.1109/TGRS.2021.3123122](https://doi.org/10.1109/TGRS.2021.3123122).
- [36] J. M. Hernandez-Lobato and R. Adams, "Probabilistic backpropagation for scalable learning of Bayesian neural networks," in *Proc. 32nd Int. Conf. Mach. Learn.*, 2015, pp. 1861–1869.



Zhen Liu was born in 1995. He received the bachelor's degree in exploration technology and engineering from Southwest Petroleum University, Chengdu, China, in 2018. He is currently pursuing the Ph.D. degree in geological resources and geological engineering with China University of Petroleum (East China), Qingdao, China.

From April 2023 to January 2024, he was funded by European Union (EU) Erasmus + Program for academic exchange at Transilvania University of Brașov, Brașov, Romania. His research focuses on

the theoretical development and practical application of artificial intelligence and physics-informed neural networks (PINNs), as well as quantum computing and quantum intelligence technologies, in oil and gas exploration and geophysical reservoir interpretation. His main research interests include geophysical modeling methods that integrate data-driven approaches with physical constraints, intelligent inversion techniques for reservoir prediction, trustworthy artificial intelligence systems with reasoning capabilities and uncertainty quantification, and pioneering international applications of quantum intelligence in geophysical inversion and hydrological forecasting. In complex geological environments, he is committed to developing multisource integrated inversion frameworks that balance accuracy, interpretability, and robustness, aiming to advance intelligent sensing, cognitive decision-making, and frontier quantum technologies in geophysical exploration.

Mr. Liu was awarded the SEG Travel Grant from the Society of Exploration Geophysicists in 2025.

Junhua Zhang, photograph and biography not available at the time of publication.

Yongrui Chen, photograph and biography not available at the time of publication.

Deyong Feng, photograph and biography not available at the time of publication.

Liang Qi, photograph and biography not available at the time of publication.